The murine meninges acquire lymphoid tissue properties and harbour autoreactive B cells during chronic *Trypanosoma brucei* infection

Juan F. Quintana[1,2,3†], Matthew C. Sinton[1], Praveena Chandrasegaran[1], Lalit Kumar Dubey[4], John Ogunsola[1], Moumen Al Samman[1], Michael Haley[2,3], Gail McConnell[5], Nono-Raymond Kuispond Swar[6], Dieudonne Mumba Ngoyi[6], Neil A. Mabbott[7*], Annette MacLeod[1*]

[1]Wellcome Centre for Integrative Parasitology (WCIP). University of Glasgow, Glasgow, UK. School of Biodiversity, One Health, Veterinary Medicine (SBOHVM), College of Medical, Veterinary and Life Sciences, University of Glasgow, Glasgow UK. [2]Lydia Becker Institute of Immunology and Inflammation, University of Manchester, UK. [3]Division of Immunology, Immunity to Infection and Health, Manchester Academic Health Science Centre, University of Manchester, UK. [4]Queen Mary University of London, London, UK.[5]Stratchclyde Institute of Pharmacy and Biomedical Sciences (SIPBS), University of Strathclyde, Glasgow, UK. [6]Department of Parasitology, National Institute of Biomedical Research, Kinshasa, Democratic Republic of the Congo. [7]The Roslin Institute and Royal (Dick) School of Veterinary Studies, University of Edinburgh, Edinburgh, UK.

[*] These authors contributed equally

[†]Corresponding author: juan.quintana@glasgow.ac.uk

Keywords: sleeping sickness, African trypanosomes, neuroinflammation, meninges, fibroblasts.

Running title: Functional characterisation of the murine meninges during chronic infections

Abstract

The meningeal space is an important structure in the brain borders, which provides immunosurveillance for the central nervous system, but the impact of infections on the meningeal immune landscape is far from being fully understood. The extracellular protozoan parasite *Trypanosoma brucei*, which causes Human African Trypanosomiasis (HAT) or sleeping sickness, accumulate in the meningeal spaces, ultimately inducing severe meningitis and resulting in death if left untreated. Thus, sleeping sickness represents an attractive model to study immunological dynamics in the meninges during infection. Here, combining single cell transcriptomics and mass cytometry by time of flight (CyTOF), coupled with *in vivo* interventions, we found that chronic *T. brucei* infection triggers the development of ectopic lymphoid aggregates (ELAs) in the murine meninges during chronic infection. These infection-induced ectopic structures are defined by the presence of ER-TR7^{+} fibroblastic reticular cells (FRCs) and follicular dendritic cells (FDCs) that initiate a signalling cascade driving local T cell activation towards a T follicular helper (T_{FH})-like phenotype, as well as B cell class switching. Furthermore, the GC-like B cells found in the infected meninges produce high-affinity autoantibodies able to recognise mouse brain antigens. We found that systemic lymphotoxin β (LTβ) signalling blockade led to a significant depletion of meningeal FDC-like cells and autoreactive B cells, indicating that LTβ signalling is critical to induce and maintain local responses in the meninges. In humans, we identified the presence of autoreactive IgG antibodies able to recognise human brain lysates in the cerebrospinal fluid of second stage HAT patients compared to first stage HAT patients, consistent with our findings in experimental infections. Taken together, our data provide evidence that the meningeal immune response results in the acquisition of lymphoid tissue-like properties during chronic *T. brucei* infection, broadening our understanding of meningeal immunity in the context of chronic infections. These findings have wider implications for understanding the mechanisms underlying the formation ELAs during chronic inflammation resulting in autoimmunity in mice and humans, as observed in other autoimmune neurodegenerative disorders such as neuropsychiatric lupus and multiple sclerosis.

Introduction

The meningeal space is rapidly emerging as a critical site for immunological responses in the central nervous system (CNS) under homeostasis[1–3], aging[4], and as a consequence of insults such as traumatic brain injury[5] and infection[6–8]. The extracellular protozoan parasite *Trypanosoma brucei*, which causes human African trypanosomiasis or sleeping sickness in humans, and animal African trypanosomiasis or nagana in domestic animals accumulates in the CNS and meningeal spaces triggering severe meningitis[9,10], culminating in the development of a wide range of debilitating neurological disorders[9,11–13]. These symptoms are diverse and include fatigue, altered sleep and circadian patterns, tremors, motor weakness, epilepsy, paralysis of one or more extremities, and Parkinson-like abnormal body movements[14–16]. Consistent with clinical data from humans, experimental trypanosomiasis in mice also results in chronic infection, leading to altered behaviour[17–20]. Thus, murine infection with *T. brucei* is a useful model to investigate meningeal responses to infection.

Chronic inflammatory processes are known to result in the formation of ectopic lymphoid aggregates (ELAs)[21–24]. Indeed, ELAs have been reported in a wide range of autoimmune disorders, including those affecting the CNS, such as neuropsychiatric lupus[25] and multiple sclerosis[26]. The diverse cytokine and chemokine repertoire found in chronically inflamed tissues, including the upregulated expression of cytokines such as lymphotoxin-α/-β (LTα and LTβ) and the chemokine CXCL13, help to create interactive niches needed to generate such structures[21–24]. Stromal LTβ receptor (LTβR) signalling is important in generating the microarchitecture required for efficient antigen presentation and follicle organisation, which typically includes collagen-rich reticular cords that serve as channels for cellular trafficking, immunological synapses, and B cell affinity maturation[27]. Similarly, CXCL13 is an important chemokine for defining local gradients controlling B cell domains, typically in proximity to follicular dendritic cells (FDCs) and follicular helper $CD4^+$ T cells (T_{FH}) inducing the formation of germinal centres, in which B cells undergo affinity maturation and somatic hypermutation to generate high affinity antibodies[21,23,25]. These reactions are typically restricted to secondary lymphoid organs such as the spleen and lymph nodes, but can occur ectopically in response to chronic inflammation, and may result in pathological

consequences such as the formation of autoreactive antibodies, as recently described for multiple sclerosis and neuropsychiatric lupus[23,25,26,28].

In secondary lymphoid organs, including the spleen and lymph nodes, lymphatic vessels act as conduits for the transport of tissue-derived antigens and dendritic cells to lymph nodes, where naïve and memory T cells are optimally positioned for the detection of their cognate antigen[29–31]. Similarly, immune complexes can be acquired by macrophages in the subcapular space in lymph nodes and transferred directly to FDCs and B cells[32]. However, several key findings in recent years have led to a better understanding of the role of lymphatic vessels in the dura matter layer of the meninges. For instance, the meningeal lymphatic vessels can convey macromolecular complexes and immune cells from the meninges and cerebrospinal fluid (CSF) to the deep cervical lymph nodes[4,33,34], although it is also plausible that extramedullary reactions may take place locally in the meningeal spaces and brain borders, as reported recently in neuropsychiatric lupus[25] and multiple sclerosism[28]. However, it is unclear whether the same extramedullar immunological reactions in the brain and/or meninges, reminiscent of those taking place in secondary lymphoid tissues, can be triggered by chronic, unresolved infections.

Here, we investigated how the meningeal transcriptional environment is altered during chronic *T. brucei* infection, using a combination of single cell transcriptomics and mass cytometry by time-of-flight (CyTOF). We found that chronic *T. brucei* infection in the meningeal space results in a broad rearrangement of the immune landscape in the murine meninges upon infection, with a significant increase in the frequency of innate (mononuclear phagocytes and granulocytes) and adaptive (T, NKT, and B cells) immune cells. Furthermore, we identified a population of autoreactive B cells in the meningeal spaces, including the leptomeninges, able to recognise mouse brain antigens and deposit high-affinity IgG antibodies in several brain areas including the hippocampus and cortex, and is associated with cortical and white matter demyelination. We also detected significant levels of autoreactive IgM and IgG antibodies in the cerebrospinal fluid of HAT patients with inflammatory encephalopathy. Taken together, this study demonstrates that the meningeal landscape acquires lymphoid tissue-like properties and supports local T and B cell activation, aided by both the meningeal stroma fibroblast and resident myeloid cells, resulting in the formation of autoreactive B cells. These results imply that chronic brain inflammation by African trypanosomes results in an autoimmune disorder affecting the brain as observed in

other neurological disorders of unknown aetiology such as neuropsychiatric lupus and multiple sclerosis. We anticipate that the data presented here will pave the way to understanding how chronic meningitis results in impaired peripheral tolerance and the development of autoimmunity in the context of chronic infections.

Materials and methods

Ethical statement. All animal experiments were approved by the University of Glasgow Ethical Review Committee and performed in accordance with the home office guidelines, UK Animals (Scientific Procedures) Act, 1986 and EU directive 2010/63/EU. All experiments were conducted under SAPO regulations and UK Home Office project licence number PP4863348 to Annette Macleod. The *in vivo* work presented in this study was conducted at 30-days post-infection (dpi) and correlated with increased clinical scores and procedural severity. The use of human biofluids was approved by the University of Glasgow MVLS Ethics Committee for Non-Clinical Research Involving Human Subjects (Reference no. 200120043).

Murine infections with *Trypanosoma brucei*. Six- to eight-week-old female C57BL/6J mice (JAX, stock 000664) were inoculated by intra-peritoneal injection with ~2 x 10^3 parasites of strain *T. brucei brucei* Antat 1.1E[35]. Parasitaemia was monitored by regular sampling from tail venesection and examined using phase microscopy and the rapid "matching" method[36]. Uninfected mice of the same strain, sex and age served as uninfected controls. Mice were fed *ad libitum* and kept on a 12 h light–dark cycle. All the experiments were conducted between 8h and 12h. For sample collection, we focussed on 30 days post-infection, as this has previously been shown to correlate with parasite infiltration in the epidural space[10,11]. Culture-adapted *T. brucei* Antat 1.1E whole cell lysates were prepared as followed. Parasites were cultured in HMI-9 supplemented with 10% FBS and 1% Penicillin/Streptomycin were grown at 37°C and 5% CO_2 and harvested during the log phase. The parasites were harvested by centrifugation (800 g for 10 min at 4°C), washed three times in 1X PBS (Gibco) supplemented with cOmplete protease Inhibitor cocktail (Roche), and sonicated with 5 pulses of 10 seconds each. The resulting lysate was cleared by centrifugation (3,000g for 10 min at 4°C to remove cell debris), and the protein concentration of the cleared supernatant was measured using the Qubit protein kit (Thermo) and kept at -80°C until usage for ELISPOT and ELISA. For LTBR-Ig treatment, mice were inoculated with 1μg/μL of either LTBR-Ig or IgG2a i.p. (100 μl/mouse) for four consecutive days prior to

infection, and then every seven days post-infection until culling. Preparation of single cell suspension from skull meninges for single-cell RNA sequencing

Tissue processing and preparation of single cell suspension. Single-cell dissociations for scRNAseq experiments were performed as follow. Animals were infected for 30 days (*n* = 2 mice/pool, 2 independent pools per experimental condition), after which skullcap meninges were harvested for preparation of single cell suspensions. Uninfected animals were also included as naive controls (*n* = 3 mice/pool, 2 pools analysed). Briefly, all mice were killed by rapid decapitation following isoflurane anaesthesia, within the same time (between 7:00 and 9:00 AM). The excised meninges were enzymatically digested with Collagenase P (1 mg/ml) and DNAse I (1 mg/ml; Sigma) in 1X PBS (HSBB) (Invitrogen) for ~30 min at 37 °C. Single-cell suspensions were passed through 70 µm nylon mesh filters to remove any cell aggregates, diluted to ~1,000 cells/µl (in 1X phosphate buffered saline supplemented with 0.04% BSA), and kept on ice until single-cell capture using the 10X Chromium platform. The single cell suspensions were loaded onto independent single channels of a Chromium Controller (10X Genomics) single-cell platform. Briefly, ~25,000 single cells were loaded for capture using 10X Chromium NextGEM Single cell 3 Reagent kit v3.1 (10X Genomics). Following capture and lysis, complementary DNA was synthesized and amplified (12 cycles) as per the manufacturer's protocol (10X Genomics). The final library preparation was carried out as recommended by the manufacturer with a total of 14 cycles of amplification. The amplified cDNA was used as input to construct an Illumina sequencing library and sequenced on a Novaseq 6000 sequencers by Glasgow polyomics.

Read mapping, data processing, and integration. For FASTQ generation and alignments, Illumina basecall files (*.bcl) were converted to FASTQs using bcl2fastq. Gene counts were generated using Cellranger v.6.0.0 pipeline against a combined *Mus musculus* (mm10) and *Trypanosoma brucei* (TREU927) transcriptome reference. After alignment, reads were grouped based on barcode sequences and demultiplexed using the Unique Molecular Identifiers (UMIs). The mouse-specific digital expression matrices (DEMs) from all six samples were processed using the R (v4.1.0) package Seurat v4.1.0[37]. Additional packages used for scRNAseq analysis included dplyr v1.0.7, RColorBrewer v1.1.2 (http://colorbrewer.org), ggplot v3.3.5, and sctransform v0.3.3[38]. We initially captured 20,621 cells mapping specifically against the *M. musculus* genome

across all conditions and biological replicates, with an average of 30,407 reads/cell and a median of ~841 genes/cell (**S1 Table and S1A Figure**). The number of UMIs was then counted for each gene in each cell to generate the digital expression matrix (DEM). Low quality cells were identified according to the following criteria and filtered out: *i*) nFeature <200 or >4,000 genes, *ii*) nCounts <200 or >4,000 reads, *iii*) >20% reads mapping to mitochondrial genes, and *iv*) >40% reads mapping to ribosomal genes, v) genes detected < 3 cells. After applying this cut-off, we obtained a total of 19,690 high quality mouse-specific cells with an average of 950 genes/cell (**S1 Table and S1B Figure**). High-quality cells were then normalised using the *SCTransform* function, regressing out for total UMI and genes counts, cell cycle genes, and highly variable genes identified by both Seurat and Scater packages, followed by data integration using *IntegrateData* and *FindIntegrationAnchors*. For this, the number of principal components were chosen using the elbow point in a plot ranking principal components and the percentage of variance explained (30 dimensions) using a total of 5,000 genes, and SCT as normalisation method.

Cluster analysis, marker gene identification, sub-clustering, and cell-cell interaction analyses. The integrated dataset was then analysed using *RunUMAP* (10 dimensions), followed by *FindNeighbors* (10 dimensions, reduction = “pca”) and *FindClusters* (resolution = 0.7). The resolution was chosen based on in silico analysis using *Clustree*[39] (**S1C Figure**). With this approach, we identified a total of 19 cell clusters The cluster markers were then found using the *FindAllMarkers* function (logfc.threshold = 0.25, assay = “RNA”). To identify cell identity confidently, we employed a supervised approach. This required the manual inspection of the marker gene list followed by and assignment of cell identity based on the expression of putative marker genes expressed in the unidentified clusters. This was particularly relevant for immune cells detected in our dataset that were not found in the reference atlases used for mapping. A cluster name denoted by a single marker gene indicates that the chosen candidate gene is selectively and robustly expressed by a single cell cluster and is sufficient to define that cluster (e.g., *Cd79a, Cd4, C1qa, Cldn5*, among others). When manually inspecting the gene markers for the final cell types identified in our dataset, we noted the co-occurrence of genes that could discriminate two or more cell types (e.g., DCs, mononuclear phagocytes, fibroblasts). To increase the resolution of our clusters to help resolve potential mixed cell populations embedded within a single cluster and, we subset fibroblasts, DCs, and mononuclear phagocytes and analysed

them individually using the same functions described above. In all cases, upon subsetting, the resulting objects were reprocessed using the functions *FindVariableFeatures, RunUMAP, FindNeighbors*, and *FindClusters* with default parameters. The number of dimensions used in each cased varied depending on the cell type being analysed but ranged between 5 and 10 dimensions. Cell type-level differential expression analysis between experimental conditions was conducted using the *FindMarkers* function (*min.pct* = 0.25, *test.use* = Wilcox) and (*DefaultAssay* = "SCT"). For cell-cell interaction analyses, we used CellPhoneDB[40] and NicheNet[41] with default parameters using "mouse" as a reference organism, comparing differentially expressed genes between experimental conditions (*condition_oi* = "Infected", *condition_reference* = "Uninfected"). Pathways analysis for mouse genes were conducted using STRING [26] with default parameters. Module scoring were calculated using the *AddModuleScore* function to assign scores to groups of genes of interest (*Ctrl* = 100, *seed* = NULL, *pool* =NULL), and the scores were then represented in feature plots. This tool measures the average expression levels of a set of genes, subtracted by the average expression of randomly selected control genes. The complete gene list used for module scoring derived from previous publications[25] or from the MatrisomeDB[42]. Once defined, the collated gene list was used to build the module scoring. Raw data and scripts used for data analysis will be made publicly available after peer review.

Whole mount meningeal preparation and immunofluorescence. Formalin-fixed paraffin embedded coronal brain sections were section on a microtome (Thermo) and fixed in 4% PFA for 10 min at room temperature. Sections were blocked with blocking buffer (1X PBS supplemented with 5% foetal calf serum and 0.2% Tween 20) and incubated with the following primary antibodies at 4°C overnight: REAfinity anti-mouse FITC CD21/35 (Miltenyi, 1:50), rat anti-mouse ER-TR7 (Novus Biologicals, 1:100), REAfinity anti-mouse PE CD3 (Miltenyi, 1:100), REAfinity anti-mouse APC B220 (Miltenyi, 1:100), anti-mouse CD138 PE (BD Bioscience, 1:100). For the detection of ER-TR7, we used an anti-rat antibody coupled with PE (Thermo, 1:500) for 1 hour at room temperature. All the antibodies were diluted in blocking buffer. Slides were mounted with Vectashield mounting medium containing DAPI for nuclear labelling (Vector Laboratories) and were visualized using an Axio Imager 2 (Zeiss).

Single molecule fluorescent *in situ* hybridisation (smFISH) experiments were conducted as follow. Briefly, to prepare tissue sections for smFISH, infected animals and naïve

controls were anesthetized with isoflurane, decapitated and the skull caps containing the dura mater layer of the meninges were dissected and place on ice-cold 1X HBSS. The skulls were then fixed with 4% paraformaldehyde (PFA) at 4 °C for 15 min, and then dehydrated in 50, 70 and 100% ethanol. After fixation, the skulls caps were decalcified, cut coronally and embedded in paraffin. 5 µm skull cap sections were RNAscope 2.5 Assay (Advanced Cell Diagnostics) was used for all smFISH experiments according to the manufacturer's protocols. We used RNAscope probes against mouse Podoplanin on channel 1 (*Pdpn*; Cat. No 437771) and *Cxcl13* on channel 2 (Cat. No. 406311-C2). All RNAscope smFISH probes were designed and validated by Advanced Cell Diagnostics. For image acquisition, 16-bit laser scanning confocal images were acquired with a 63x/1.4 plan-apochromat objective using an LSM 710 confocal microscope fitted with a 32-channel spectral detector (Carl Zeiss). Lasers of 405nm, 488nm and 633 nm excited all fluorophores simultaneously with corresponding beam splitters of 405nm and 488/561/633nm in the light path. 9.7nm binned images with a pixel size of 0.07um x 0.07um were captured using the 32-channel spectral array in Lambda mode. Single fluorophore reference images were acquired for each fluorophore and the reference spectra were employed to unmix the multiplex images using the Zeiss online fingerprinting mode. All fluorescent images were acquired with minor contrast adjustments where needed, and converted to grayscale, to maintain image consistency.

Flow cytometry analysis and *ex vivo* stimulation of meningeal-dwelling T cells. To discriminate circulating versus brain-resident immune cells, we performed intravascular staining of peripheral $CD45^+$ immune cells, as previously reported[43]. Briefly, a total of 2 µg of anti-CD45-PE antibody (in 100 µl of 1X PBS) was injected intravenously 3 minutes prior culling. Mice were euthanised as described above and transcardially perfused with ice-cold 0.025% (wt/vol) EDTA in 1X PBS. Whole brain samples were collected and placed on ice-cold 1X HBSS (Invitrogen). Whole meninges were enzymatically digested with Collagenase P (1 mg/ml) and DNAse I (1 mg/ml; Sigma) in 1X PBS (HSBB) (Invitrogen) for ~30 min at 37 °C, according to previously published protocols[44]. Single-cell suspensions were passed through 70 µm nylon mesh filters to remove any cell aggregates. The cell suspension was cleaned up and separated from myelin debris using a Percoll gradient. The resulting fraction was then gently harvested and used as input for *ex vivo* T cell stimulation. Briefly, the resulting cell fraction was

diluted to a final density of ~1x10^6 cells/ml and seeded on a 96 well plate and stimulated with 1X cell Stimulation cocktail containing phorbol 12-myristate 13-acetate (PMA), Ionomycin, and Brefeldin A (eBioSciences^{TM}) for 5 hours at 37°C and 5% CO_2. Upon stimulation, the cells were analysed for the expression of IL-21 and PD-1.

For flow cytometry analysis, meningeal single cell suspensions were resuspended in ice-cold FACS buffer (2 mM EDTA, 5 U/ml DNAse I, 25 mM HEPES and 2.5% Foetal calf serum (FCS) in 1X PBS) and stained for extracellular markers. The list of flow cytometry antibodies used in this study were obtained from Biolegend and are presented in the table below. Samples were run on a flow cytometer LSRFortessa (BD Biosciences) and analysed using FlowJo software version 10 (Treestar). For intracellular staining, single-cell isolates from brain were stimulated as above in Iscove's modified Dulbecco's media (supplemented with 1X non-essential amino acids, 50 U/ml penicillin, 50 µg/ml streptomycin, 50 µM β-mercaptoethanol, 1 mM sodium pyruvate and 10% FBS. Gibco). Cells were then permeabilized with a Foxp3/Transcription Factor Staining Buffer Set (eBioscience) and stained for 30 min at 4 °C. The anti-mouse GP38 (1:100) and the LTβ (monoclonal antibody BBF6[45]; 10 µg/ml) antibodies were kindly provided by Dr. Lalit Kumar Dubey (QMUL). For the detection of LTβ in CD4$^+$ T cells, we used a goat anti-hamster (Armenian) IgG coupled to FITC as secondary antibody (Biolegend; 1:200). For the detection of GP38 we used an Syrian hamster-anti mouse GP38 followed by anti-Syrian hamster secondary antibody coupled to APC/alexa647 (Jackson ImmunoResearch; 1:100).

Supplier	**Target**	**Fluorophore**	**Clone**	**Dilution**
Biolegend	TER-119	PE-Cy7	TER-119	1:400
Biolegend	CD19	PE-Cy7	1D3/CD19	1:400
Biolegend	F4/80	PE-Cy7	BM8	1:400
Biolegend	CD3	APC	17A2	1:400
Biolegend	CD4	FITC	GK1.5	1:400
Biolegend	PD1	BV711	29F.1A12	1:400
Biolegend	CXCR5	BV421	L138D7	1:200
Biolegend	IL-21	PE	3A3-N2	1:200
Biolegend	CD45	PE	QA17A26	1:400
Biolegend	CD31	BV421	8.1.1	1:100
Biolegend	CD21/35	PE Dazzle 594	7E9	1:100

Biolegend	MAdCAM-1	Alexa Fluor 488	MECA-367	1:100
Biolegend	CD19	Alexa Fluor 488	6D5	1:400
Biolegend	CD138	PE	281-2	1:200
Biolegend	IgG	BV421	Poly4053	1:200
Biolegend	IgM	BV711	RMM-1	1:200
Biolegend	CD8a	BV421	QA17A07	1:400
Biolegend	I-A/I-E	BV605	M5/114.15.2	1:400

Mass cytometry sample processing

Single cell suspension from meninges were prepared as described above and resuspended in Dubecco's Modified Eagle Medium (DMEM) to a concentration of 1 x 10^6 cells/mL. Cells were activated for 6 h in a round-bottom 96-well plate using Cell Activation Cocktail (containing with Brefeldin A) (BioLegend, San Diego, USA) as per the manufacturer's recommendations. Plates were then centrifuged at 300 x g for 5 min and the pellets resuspended in 50 µL of Cell-ID™ Cisplatin-195Pt viability reagent (Standard BioTools, San Francisco, USA), and incubated at room temperature for 2 min. Cells were washed twice in Maxpar® Cell Staining Buffer (Standard BioTools, San Francisco, USA), and centrifuged at 300 x g at room temperature for 5 min. The CD16/CD32 receptors were then blocked by incubating with a 1/50 dilution of TruStain FcX™ (BioLegend, San Diego, USA) in PBS at room temperature for 15 min. An antibody cocktail was prepared from the Maxpar® Mouse Sp/LN Phenotyping Panel Kit (Standard BioTools, San Francisco, USA), with and additional antibody against IgM. Cells were incubated with antibodies for 60 min, on ice before washing 3 times in Maxpar® Cell Staining Buffer (Standard BioTools, San Francisco, USA) as previously. Following staining, cells were fixed in 2% paraformaldehyde (PFA) overnight at 4°C. Cells were then washed twice with 1X eBioscience™ Permeabilization Buffer (Invitrogen, Waltham, USA) at 800 x g at room temperature for 5 min. The pellets were resuspended in intracellular antibody cocktail and incubated at room temperature for 45 min. Cells were washed 3 times in Maxpar® Cell Staining Buffer (Standard BioTools, San Francisco, USA) at 800 x g. The cells were then resuspended in 4% PFA at room temperature for 15 min, before collecting the cells at 800 x g and resuspending in Cell-ID™ Intercalator-Ir (Standard BioTools, San Francisco, USA). Finally, the cells were barcoded by transferring the stained cells to a fresh tube containing 2 µL of palladium barcode from the Cell-ID™ 20-Plex Pd Barcoding Kit (Standard BioTools, San

Francisco, USA). Cells were then frozen in a freezing solution (90% FBS and 10% DMSO), before shipping to the Flow Cytometry Core Facility at the University of Manchester for data acquisition. The list of antibodies used is listed below. Sample analysis was conducted using Cytobank and custom-built, python-based analysis scripts developed in house.

Surface Antibodies				
Antibody	**Metal Conjugate**	**Clone**	**Concentration**	**Cat. No.**
Ly6G/C [Gr1]	141Pr	RB6-8C5	1/100	201306
CD11c	142Nd	N418	1/100	
CD69	145Nd	H1.2F3	1/100	
CD45	147Sm	30-F11	1/200	
CD11b	148Nd	M1/70	1/100	
CD19	149Sm	6D5	1/100	
CD3e	152Sm	145-2C11	1/100	
TCRβ	169Tm	H57-597	1/100	
CD44	171Yb	IM7	1/100	
CD4	172Yb	RM4-5	1/100	
IgM	151Eu	RMM-1	1/100	
Intracellular Antibodies				
IFNγ	165Ho	XMG1.2	1/100	3165003B

ELISPOT assays

ELISPOT tests to measure *ex vivo* the frequency of meningeal antibody secreting cells (ASCs) was performed using the ELISpot Flex IgM- and IgG-HRP (Mabtech) as followed. After generating single cell suspensions from meningeal preparations, a total of 50,000 cells per well were seeded on 96-wells multiscreen-HA filter plates (Millipore) coated with 50 μg/ml of either whole *T. brucei*, prepared in house, or mouse brain lysate (Novus Biologicals) to determine the presence of *T. brucei*- and mouse brain-reactive antibody secreting cells, respectively. Wells coated with 50 μg/ml BSA (Sigma) were also included as negative controls. After seeding the cells, the plates were incubated for 16 hours at 37°C, and 5%CO_2 covered in foil to avoid evaporation. In parallel, plates coated with 15 μg/ml affinity-purified goat anti-mouse IgM and IgG were also analysed in parallel to measure the frequency of total IgM and IgG ASCs. For this,

we used a total of 25,000 cells per well and incubated as before. Spots were enumerated with an Immunospot analyser (CTL, Germany).

Detection of autoreactive IgM and IgG by ELISA

Serum samples from naïve and infected animals at 30 days post-infection were used to examine the presence of mouse brain lysate-specific IgM and IgG using a colorimetric approach. For this purpose, polysorb ELISA plates (Biolegend) were coated overnight with 50 µg/ml either *T. brucei* Antat 1.1E whole cell lysate prepared in house, or mouse brain lysate (Novus Biologicals) in 1X coating buffer (Biolegend). After extensive washes with 1X ELISA washing buffer (Biolegend), total mouse IgM or IgG were detected in mouse serum (1:50 to 1:10,000 dilution in 1X PBS) or human CSF (1:400 in 1X PBS) by using Horseradish peroxidase-conjugated antibodies specific for mouse IgM (Thermo) or IgG (all isotypes; Sigma) using the recommended concentrations, and the resulting absorbance was detected at 450 nm using an ELISA Multiskan plate reader (Thermo).

Data availability

The transcriptome data generated in this study have been deposited in the Gene Expression Omnibus (GSE229436). The processed transcript count data and cell metadata generated in this study, as well as the code for analysis, are available at Zenodo (DOI: 10.5281/zenodo.7814657). Additional data and files can also be sourced via Supplementary Tables.

Code availability

The processed transcript count data and cell metadata generated in this study, as well as the code for analysis, are available at Zenodo (DOI: 10.5281/zenodo.7814657).

Statistical analysis

All statistical analyses were performed using Graph Prism Version 8.0 for Windows or macOS, GraphPad Software (La Jolla California USA). The data distribution was determined by normality testing using the Shapiro-Wilks test. Where indicated, data were analysed by unpaired Student's t-test, Mann-Whitney test, or one-way analysis of variance (ANOVA). Data were considered to be significant where $p < 0.05$. For the *in vivo* experiments, we matched sex and age of the mice in experimental batches using a block design including randomisation of experimental units. Data collection and analysis were not performed blindly to the conditions of the experiment due to specific requirements in the animal license.

Results

The murine skull meninges are colonised by a diversity of immune cells during chronic *T. brucei* infection

We and others have shown an increase in meningeal infiltration and meningitis during the chronic stage (25dpi onwards) in experimental infections with *T. brucei*[10,13]. Previous studies have shown that mouse meninges are colonised by $CD2^+$ T cells and $CD11c^+$ dendritic cells (DCs) during chronic *T. brucei* infection[9], although a catalogue of the immune interactions spanning beyond these compartments is lacking. To fill this gap in knowledge, we used an integrative multi-omics approach, combining CyTOF and 10X Chromium single cell transcriptomics (**Figure 1A**) to understand the complexity of the immune interactions taking place in the meningeal space during chronic *T. brucei* infection. In addition to unbiasedly cataloguing the cells involved in this process, this approach also allowed us to identify transcriptional pathways involved in the anti-parasitic responses in the meninges with as much singularity as possible. To make sure we captured the diversity of resident immune cells and meningeal stroma with as much confidence as possible, we selectively removed all circulating $CD45^+$ immune cells using a magnetic sorting approach (**Figure 1A**). In brief, we labelled circulating $CD45^+$ cells by intravenous injection with an anti-$CD45^+$ antibody coupled to phycoerythrin (PE). All the circulating $CD45^+$ were then isolated using an anti-PE antibody coupled to magnetic beads. After extensive perfusion, we removed all the remaining circulating (PE^+ cells) cells leaving behind resident $CD45^+$ cells (PE^- cells), as well as stromal cells, including fibroblasts and cells associated with the vasculature and the lymphatic system. Firstly, we decided to explore the broad immunological landscape in the

meninges of mice at 30dpi, when infection in the central nervous system is well established[9–13]. For this reason and given the scarcity of cells typically obtained from the meninges, we decided to use CyTOF as this approach enables detection of a wide range of cell types. Overall, we detected a significant increase in the number of $CD45^+$ cells in the murine meninges at 30dpi compared to naïve controls (**Figure 1A to 1D**). These included $CD11b^+$ macrophages and $Ly6G^+$ granulocytes, conventional ($CD3\varepsilon^+$ $TCR\beta^+$) $CD4^+$ and $CD8^+$ T cells, γδ T cells, NK cells, and B cells (including IgM^+ and $CD11c^+$ B cells) in the murine meninges (**Figure 1E**), consistent with previous work[2]. At 30dpi, we detected a significant increase in the frequency of meningeal $CD4^+$ and $CD8^+$ T cells (including $IFN\gamma^+$ $CD4^+$ T cells), macrophages, and B cells (including IgM^+ B cells) compared to naïve controls, without noticeable changes in the frequency of granulocytes, γδ T cells, NK cells, and $CD11c^+$ B cells (**Figure 1F**).

To gain an understanding of the transcriptional responses triggered in the meninges in response to infection, and to identify potential interactions between various meningeal cells during infection, we performed single cell RNA sequencing of meningeal preparations from mice at 30 dpi (*n* = 2 pools; 2 mice/pool) and naive controls (*n* = 2 pools; 2 mice/pool). Using this approach and after removing cells catalogued as low quality (**Materials and Methods**), we obtained a total of 19,690 high quality cells, from which 1,834 cells derived from naïve meninges and 17,856 cells from infected meninges, with an average of 605 genes per cell from naïve samples and 1,297 genes per cell from infected samples (**Figure 2A, Figure S1, and Materials and Methods**). As expected, our single cell meningeal atlas encompasses stromal and immune cells, most of which have previously been reported in the murine meninges[2,46]. Within the stromal compartment, we identified two populations of *Col1a1*$^+$ fibroblasts, *Notch3*$^+$ mural cells, and *Pecam1*$^+$ endothelial cells (**Figure 2A to 2C, and S2 Table**). Within the immune compartment, we identified five populations of mononuclear phagocytes (MNPs 1 to 5), characterised by the expression of putative myeloid cell markers genes such as *Ccl8, C1qa, Aif1, Adgre1* and *Cd14*, amongst others, as well as conventional DCs (cDCs) expressing high levels of *Xcr1, Zbtb46, Clec9a, Flt3* and *Itgae* (**Figure 2A to 2C, and S2 Table**). Additionally, we also detected *Cd4*$^+$ and *Cd8*$^+$ T cells, *S100a8*$^+$ granulocytes (including *Ngp*$^+$ neutrophils), and two populations of B cells (**Figure 2A to 2C, and S2 Table**). Lastly, we detected a small proportion of cells (>0.5%) with high expression levels of haemoglobin (*Hba-a1, Hbb-bt*) and genes typically related to

neurons (*Neurod1, Neurod4*) (**Figure 2A to 2C, and Table S2**). Notably, we observed a robust increase in the frequency of most of the cells within the immune compartment (**Figure 2C**) consistent with the CyTOF dataset. Together, these analyses are consistent with profound alterations in the cellular makeup of the murine meninges during chronic *T. brucei* infection.

Meningeal fibroblasts acquire lymphoid tissue stroma-like properties during chronic *T. brucei* infection.

Next, we focussed on the meningeal fibroblasts. The meningeal fibroblasts are a heterogeneous cell population encompassing transcriptionally, spatially, and potentially functionally distinct units critical for meningeal immunity[47–50], but their responses to chronic protozoan infections remains to be elucidated. Therefore, we first asked whether the three fibroblast clusters (Fibroblast 1, Fibroblast 2, and myofibroblasts) identified in figure 1 contained discreet clusters not resolved at the top clustering level. After sub-clustering, we identified 2,088 cells (547 and 1,541 cells from naïve and infected meningeal preparations, respectively), distributed across eight discrete subsets (**Figure 3A**). These clusters expressed marker genes putatively associated with fibroblasts from the dura matter, including *Mgp, Gja1, Fxyd5 and Col18a1*, but low levels of other marker genes recently identified in pia matter (*Lama2, S100a6, Ngfr*) or arachnoid matter fibroblasts (*Crabp2, Clnd11, Tbx18, Tagln*) (**Figure 3B**)[48], indicating that the majority of these fibroblasts derived from the dura matter layer of the meninges.

Next, we focussed on the meningeal fibroblasts. A recent study demonstrated that meningeal fibroblasts are a heterogeneous cell population encompassing transcriptionally, spatially, and potentially functionally distinct units critical for meningeal immunity[47–50]. Therefore, we first asked whether the three fibroblast clusters (Fibroblast 1, Fibroblast 2, and myofibroblasts) identified in figure 1 contained discreet clusters not resolved at top clustering level. After sub-clustering, we identified 2,088 cells (547 and 1,541 cells from naïve and infected meningeal preparations, respectively), distributed across eight discrete subsets (**Figure 3A**). These clusters express marker genes putatively associated with fibroblasts from the dura matter, including *Mgp, Gja1, Fxyd5, and Col18a1*, but low levels of other marker genes recently identified in pia matter (*Lama2, S100a6, Ngfr*) or arachnoid matter fibroblasts (*Crabp2, Clnd11, Tbx18, Tagln*) (**Figure 3B**)[48], indicating that the majority of these fibroblasts derived from the dura matter layer of the meninges.

These fibroblast clusters also contained the mesenchymal markers *Col1a1, Col1a2, Pdgfra* and *Pdgfrb,* but lacked *Pecam1* (encoding for CD31) suggesting that these cells are of mesenchymal origin rather than endothelial (**Figure 3C**). Furthermore, cells within clusters 0, 1, 2, 3 and 5 expressed *Cspg4* and *Pdpn*, which encode for NG2 and GP38, respectively, suggesting that these are meningeal pericytes[50]. Additionally, cells within clusters 0, 3 and 5 also expressed *Ly6a* (which encodes for the Stem Cell antigen-1, Sca1) suggesting they are likely to retain progenitor properties[50]. Cells within cluster 6 expressed high levels of *Acta2* (which encodes for α-smooth muscle actin) and were thus classified as myofibroblasts[50]. We also found heterogeneous responses to infection within the meningeal fibroblast subset. For instance, cells within cluster 2, described as a mature population of pericytes, were exclusively detected in the infected meninges and were characterised by the expression of genes associated with blood vessel development (*Fgfr, Thbs1, Fgf2*), as well as leukocyte chemotaxis and myeloid differentiation (*Cxcl14, Ccl4, Cd74, Tirap*) (**Figure 3A, 3D, and Table S3**), suggesting *de novo* expansion in response to infection. Similarly, cluster 5 was expanded in the infected meninges and was dominated by the expression of genes typically observed in the stroma of lymphoid tissues, including *Ccl19* in addition to genes associated with the composition of the extracellular matrix, including *Mmp13, Col14a1*, *Col18a1* and *Aldh1a2*, resembling the *Aldh1a2*$^+$ fibroblastic reticular cells (FRCs) found in the omental milky spots involved in lymphocyte recruitment and local immune responses in the omentum[51] (**Figure 3A, 3D, and Table S3**). Indeed, cells within cluster 4) expressed the marker genes (*Pdpn, Pdgfra, Pdgrfb, Des, Vim*, and *Col6a3*) and secreted factors (*Il7, Vegfa , Tnfsf13b*, and *Ccl21a*) associated with FRCs (**Figure S3A**)[52], whereas cells within clusters 5 and 6 expressed marker genes of typically found in FDCs (*Tnfsf11*, encoding for RANKL, as well as *Itga7, Ltbr, Madcam1* and *Cr2*, which encodes for CD21/35) in addition to *Cxcl13* (**Figure S3B and S3C**)[52]. Additionally, all of the fibroblast subsets are involved in extracellular matrix (ECM) remodelling in the meninges, including collagen and proteoglycan deposition, secretion of factors involved in ECM production, and ECM regulators, as demonstrated by module scoring analysis using MatrisomeDB database[42] (**Figure S3D**) encompassing a curated proteomic dataset from ECM derived from wide range of murine tissues.

These results indicate that the dura matter layer of the meninges contains a diverse population of stromal cells, including GP38$^+$ and GP38$^-$ stromal cells that resemble the

stroma of other lymphoid tissues and ECM remodelling. Consistent with our scRNAseq data, using flow cytometry, we observed a significant expansion of GP38^{+} FRCs, and a distinctive population of MAdCAM1^{+} CD21/CD35^{+} cells indicative of the presence of follicular dendritic cell (FDC)-like cells in the infected murine meninges compared to naïve controls (**Figure 3E-F, and Figure S2A**). Furthermore, module scoring analysis, which allows us to assess global gene signatures associated with a gene set or pathway (in this case, ectopic lymphoid tissue signatures), suggested that cells within cluster 5 were enriched for genes associated with FDC-like function and stromal lymphoid tissues, including *Cr2, Fcgr2b, Mfge8,* and *Tnfsf13b*, compared to the other fibroblast clusters (**Figure 3G**), and may be derived from *Ly6a*$^{+}$ pericytes with a precursor capacity as previously reported[53,54]. Indeed, two of the chemokine-encoding genes coordinating the positioning of T cells and B cells within stromal lymphoid tissues, *Ccl19* and *Cxcl13*, were upregulated exclusively in cells within cluster 5 in response to infection (**Figure 3H**), which was further confirmed by *in situ* hybridisation as a population of *Cxcl13*$^{+}$ cells within the dura matter layer of the meninges (**Figure 3I**). Together, our data demonstrates the presence of a rich diverse fibroblast population, encompassing mature pericytes (clusters 1, 2), myofibroblasts (cluster 6), perivascular fibroblasts (cluster 7), and some pericytes with a *Ly6a*$^{+}$ progenitor precursor phenotype (clusters 0, 3, and 5) with FDC-like properties.

Pseudotemporal trajectory analysis in the meningeal fibroblast responses to chronic *T. brucei* infection.

We next conducted pseudotemporal trajectory inferences and pseudotime analysis using Monocle3[55] to study to study the impact of infection on gene expression within distinct meningeal fibroblast populations. When examining the resulting pseudotemporal trajectory, we observed that fibroblast subclusters 0 and 5 displayed the lowest values on the pseudotime scale, predicting that the cells within these fibroblasts subclusters may act as local precursors controlling the stromal responses to infection, coinciding with their high expression of mesenchymal precursor marker gene *Ly6a*, encoding for Sca-1 (**Figure 4A and 4B**). Cells within the fibroblast subclusters 2 (mature pericytes), 3 (mesenchymal precursor), and 6 (myofibroblasts), displayed the highest values on the pseudotime scale, indicating that the transcriptional responses observed within these clusters emerge as a consequence of infection. Indeed, most of the markers genes identified in clusters 2 and 6 are involved in *de novo* blood and lymphatic vessel development (*Fgfr, Thbs1, Fgf2)*, consistent with reports that chronic

meningeal inflammation results in angiogenesis[56]. Interestingly, the pseudotemporal reconstruction also proposed that cluster 5 acts as a "divergent" point which can be attributed to its mesenchymal precursor potential (**Figure 4A and 4B**). A closer examination of the gene expression profile over the inferred pseudotemporal trajectory revealed that *Aldh1a2, Ccl19* and *Cxcl13*, all found to be exclusively expressed by cells within cluster 5, emerged as "early" genes in the trajectory, and this expression profile was followed by genes associated with stromal rearrangement and cell-cell adhesion molecules such as *Acta2, Col6a3, Mmp13, Postn* and *Thbs1*, which were identified as "late" genes (**Figure 4C**). Interestingly, *Postn* has been proposed as a critical regulator of *Aldh1a2*$^+$ FRCs responses in the omental milky spots[51], suggesting that cluster 5 may act as a precursor-like fibroblast population in the meninges. Consistent with our *in silico* predictions and flow cytometry analysis, gene expression profile and whole mount meningeal preparations analysed by immunofluorescence revealed clusters of CD21$^+$/35$^+$ FDC-like cells in perivascular spaces (**Figure 4D**). Similarly, we detected *Col6a3* expression exclusively in clusters 0, 3, 5 and 6, clusters, which we propose to be triggered in response to infection, and this was further confirmed by the presence of ER-TR7$^+$ mesh-like structures (recently proposed to specifically bind to COL6A3[57]; **Figure 4E**) during infection but not in naïve controls. Taken together, these results indicate that during chronic infection, the dura meningeal fibroblasts acquire *Col6a3*$^+$ FRC- and *Cr2*$^+$ FDC-like features, associated with the recruitment of lymphocytes in general, and B cells in particular, *via* chemokine signalling and stromal remodelling.

Meningeal mononuclear phagocytes are involved in antigenic presentation and chemotaxis during chronic *T. brucei* infection

The cells within the myeloid compartment in the murine meninges act as a critical first line of defence against insults and were clearly expanded during the chronic stage of the infection (**Figure 1 and 2**). To resolve the myeloid cell compartment in more detail, we analysed these populations individually. In total, we obtained 10,706 cells organised into five major clusters: cluster 0 (33.8%), cluster 1 (25.04%), cluster 2 (19.7%), cluster 3 (13.4%), and cluster 4 (8.10%) (**Figure 5A**). All clusters were characterised by high expression levels of the putative marker genes *Ptprc, Lyz2*, and the major histocompatibility complex II gene *H2-Aa, Sirpa, Csf1r, Itgam, Ly6a,* and *Adgre1* (**Figure 5B and S4 Table**). These cell clusters also contained several genes previously identified as signatures for border-associated macrophages, including *Apoe, Ms4a7, Tgbf1, Clec12a, Axl, Siglec1*, and *Vcam1*[10,58] (**Figure 5B and S4 Table**). Clusters 0 and

2 also expressed high levels of *Mrc1* (encoding for CD206) and the anti-inflammatory molecule *Il18bp*, and *Siglec1* (encoding for CD169), and so we labelled these two clusters as CD206$^+$ border-associated macrophages (BAMs) (**Figure 5B and S4 Table**). Clusters 1 and 3 contain the immune sensors *Cd14* and *Tlr2*, in addition to *Mertk, Adgre1*, and *Ly6c2*, and thus we labelled these as monocyte-derived macrophages (MDMs). Lastly, cells within cluster 4 expressed high levels of mitochondrial-associated transcripts (e.g., *mt-Co1, mt-Co2, mt-Atp6*), in addition *Itgal*, *Sirpa, Cd274, Nfkbia, Sell*, and *Cd44* (**Figure 5B and S4 Table**) and thus we labelled them as metabolically active mononuclear phagocytes. Under homeostatic conditions, the murine meninges were dominated by CD206$^+$ BAMs, in agreement with previous reports[58] (**Figure 5C**). However, during infection, there was a significant expansion of monocyte-derived macrophages (MDMs) (**Figure 5C**), suggesting that the murine meninges were populated by circulating monocytes during chronic *T. brucei* infection, consistent with previous reports[10]. Cell-cell interaction analyses predicted that the myeloid compartment interacts with CD4$^+$ T cells *via* MHC-II interactions and antigenic presentation (**Figure 5D and 5E**), likely driving T cell activation locally, as previously proposed[2,10]. Indeed, we detected a significant increase in the frequency of MHC-II$^+$ CD11b$^+$ macrophages in the infected meninges compared to naïve controls (**Figure 5F and 5G**), consistent with our *in silico* predictions (**Figure 5E**). Additionally, this analysis suggested that the meningeal myeloid cells were most likely involved in chemoattraction of a wide range of immune cells, including CD4$^+$ T cells and B cells, through expression of chemokine encoding genes including *Cxcl9, Cxcl10, Cxcl12*, and *Cxcl14* (**Figure 5H and S5 Table**). Together, our results indicate that in addition to the stroma fibroblasts, the resident population of meningeal myeloid cells are expanded upon infection and drive both cell recruitment *via* chemotaxis as well as antigen presentation to CD4$^+$ T cells. Our data are consistent with and complementary to recent reports focusing on the ontogeny and dynamics of BAMs and MNPs under homeostasis[2] and during the onset and resolution of *T. brucei* infection[10].

The murine meninges contain T_{FH} cells during chronic *T. brucei* infection

The accumulation of inflammatory T cell subsets in the meninges has been reported in CNS infections with *T. brucei*[9], but their features and effector function remain unresolved. Within the resident meningeal T cell compartment, we identified four main transcriptional clusters, characterised by the expression of *Trbc1, Cd4*, and *Cd8a* (**Figure 6A and 6B**). Several of the genes observed in the CD4$^+$ T cells were putatively

associated with T_{FH} cells, including *Icos, Pdcd1* (encoding for PD-1), *Cxcr4, Ctla4, Maf*, *Nr4a1, Csf1*, as well as the cytokines *Ifng* and *Il21* (**Figure 6B**). To confirm this, we first determined whether meningeal T cells were activated *in situ* during infection using the Nur77^{GFP} reporter mice, as previously reported under homeostatic conditions[2]. In this model, GFP expression is used as a proxy for MHC-dependent TCR engagement resulting in T cell activation[59]. We observed a significant increase in the frequency of Nur77GFP$^+$ CD4$^+$ and CD8$^+$ T cells (**Figure 6E and S2B Figure**), indicating local T cell activation within the murine meninges. Next, we set out to confirm the presence of T_{FH}-like T cells in the meninges *in vivo*. To do this, we infected mice with *T. brucei* and measured the capacity of meningeal CD4$^+$ T cells to produce IL-21 and express PD-1 *ex vivo*. We noted a significant increase in the frequency of PD1$^+$ IL-21$^+$ CD4$^+$ T cells in the meninges at 30 dpi (**Figure 6C and 6D, and S2B Figure**), confirming our prediction from the gene expression profile. Taken together, these results demonstrate that, in addition to conventional cytotoxic CD8$^+$ T cells, the meningeal CD4$^+$ T cell population has undergone MHC-dependent TCR engagement promoting local responses *in situ*, most likely due to the interaction with and antigen presentation by MNPs and stromal cells. These responses are likely to provide all the necessary signals for activation and resulting in T cell differentiation towards a T_{FH}-like phenotype during chronic *T. brucei* infection.

Murine meninges are enriched in autoreactive B cells during chronic infection

Previous studies have demonstrated that B cells represent a major immune population in the meninges[41,46], although their dynamics during chronic infection are not yet understood. We previously observed the expression of *Cxcl12* in dura and arachnoid meningeal fibroblasts, which is critical for the differentiation and survival of early B cells in the bone marrow[60,61]. Thus, we next explored the diversity of B cells in our dataset. The majority of meningeal B cells detected in our dataset derived from the infected meninges (1,688 cells out of 1,742 total B cells) (**Figure 2**). These cells expressed high levels of genes associated with plasma cells such as such as *Jchain*, *Prdm1* (which encodes for BLIMP-1)*, Sdc1* (encoding CD138), *Ighm*, and *Irf4* (**Figure 7A**). We also detected genes associated with cell replication and class-switched B cells such as *Pcna, Mki67, Ub2c and Ighg2* and *Ighg3*, in addition to *Apex2, Ung, Exo1, Msh6, Polb*, and *Aicda*, although at low frequencies (1-9% of the cells within the B cell clusters) (**Figure 7A)**. These genes are critical for affinity maturation and class switching during GC reactions[62]. Flow cytometry experiments further confirmed the presence of IgG$^+$ B

674 cells in the murine meninges during chronic infection (**Figure 7B-C, and S2C Figure**).
675 Because the transcriptional signatures observed in the cells within the B cell clusters
676 are consistent with extrafollicular GC-like reactions, we next examined this at the
677 protein level using the Nur77^{GFP} reporter mouse line to measure BCR engagement
678 within the meninges. Given that Nur77^{GFP} expression in GC B cells is proposed to be
679 markedly reduced compared to activated B cells *in vivo*[63], and that *Nur77* restrains B
680 cell clonal dominance during GC reactions[64], this reporter line can be used to examine
681 extrafollicular GC-like reactions. In line with these studies, we detected significantly less
682 GFP^{+} CD19^{+} B cells during infection compared to naïve controls (**Figure 7D and 7E,**
683 **and S2C Figure**), potentially indicating that upon infection, the meningeal B cells
684 undergo GC-like reactions. Intriguingly, the meningeal Nur77-GFP^{low} cells also
685 expressed *Cd38* and *Cxcr4* but low or undetectable levels of *Cd86* (**Figure 7F**), sharing
686 many features with the dark zone (GFP^{low}) GC B cells[63]. Importantly, the dark zone of
687 the GC is enriched in interactions between B cells and FDCs driving rapid cell
688 proliferation and somatic hypermutations[65]. Consistent with this, in the spatial context,
689 we found that the meningeal B cells were located in close proximity to CD21^{+}/CD35^{+}
690 FDC-like cell clusters, and to a lesser extent to CD3^{+} T lymphocytes (**Figure 7G and S4**
691 **Figure)**, resembling those found within ectopically-induced lymphoid tissues[24]. Given
692 their physical proximity, we next explored any potential interactions between meningeal
693 B cells with local fibroblasts using cell-cell communication analyses. We observed that
694 the meningeal fibroblasts express a wide range of ligands involved in GC reactions
695 within the B cell compartment, such as *Ltb, H2-DMa, Icam1, Cxcl14*, and *Fn1* (which
696 encodes for fibronectin 1), promoting B cell transcriptional responses including an
697 upregulation of *Nfkbia, Cd44, Sod2, Nme1*, and *Cd74*, and *Notch1*, which is critical for
698 B cell activation and antibody secretion[66] (**Figure 7H and 7I**). Together, our data
699 indicates the presence of isotype-switched B cells that have undergone GC-like
700 reactions in the meningeal space, likely aided by CD21^{+}/CD35^{+} FDC-like cells.
701 The accumulation of meningeal B cells has been reported in several autoimmune
702 disorders such as neuropsychiatric lupus[25] and multiple sclerosis[28] where they are
703 responsible for the generation of autoantibodies that are linked to the pathology
704 associated with these disorders. However, it is unclear whether chronic *T. brucei*
705 infection also results in the accumulation of autoreactive B cells in the meningeal
706 spaces. We reasoned that in addition to generating B cell clones able to generate
707 antibodies specifically to *T. brucei*, these local GC-like reactions taking place within the

meningeal space might also result in the development of autoreactive B cells. To directly test this hypothesis, we examined the presence of meningeal resident IgG^+ antibody secreting cells (ASCs) able to recognise *T. brucei* and mouse brain lysates using ELISpot. We observed a significant accumulation of total IgG^+ ASCs in the murine meninges (**Figure 8A and 8B**), consistent with the flow cytometry data (**Figure 7B**). We also detected a significant accumulation of IgG^+ ASCs able to recognise *T. brucei* and mouse brain but not BSA (**Figure 8A and 8B**), indicative of the presence of autoreactive ASCs in the murine meninges during infection. Interestingly, splenocytes from animals at 30dpi or naïve controls did not contain autoreactive IgG^+ ASCs (**S5A Figure**), suggesting that the mouse brain-specific autoreactive ASCs may arise locally within the meninges (or within the CNS environment).

Histological analysis of the corresponding murine brain sections revealed extensive IgG deposition in the infected brain compared to naïve controls, in particular in the leptomeninges and the cortex (**Figure 8C**). Additionally, we detected the presence of high IgM and IgG titters in the serum of infected animals able to react to mouse brain antigens compared to naïve controls (**Figure 8D and 8E**), further corroborating our histological and ELISpot findings. It is important to note that the binding of circulating IgG antibodies to the murine brain is not restricted to areas with high parasite accumulation (e.g., lateral ventricles) (**Figure 8E**). The accumulation of autoreactive antibodies is associated with demyelination during chronic infection compared to naïve controls, particularly in the cerebral cortex, internal capsule, and thalamic tracts (**S5B and S5C Figure**). In humans, we observed significant levels of autoreactive IgM and IgG antibodies able to recognise human brain lysates, but not BSA, in the cerebrospinal fluid of 2nd stage *gambiense* HAT patients from North Uganda (**Figure 8F**), consistent with our findings in experimental infections. Taken together, our data suggest that meningeal B cells undergo affinity maturation locally within the meninges (or the CNS space) to generate IgG^+ ASCs directed against both *T. brucei* and the mouse brain (and in gambiense HAT patients), is associated with cortical and white matter demyelination, and results in autoimmunity.

LTβ receptor signalling controls the accumulation of meningeal FDCs and autoreactive B cells during chronic *T. brucei* infection.

LTβ receptor (LTβR) signalling is critical for the formation, induction, and maintenance of lymphoid tissues under homeostasis and disease[67–69]. This process requires the

interaction between LTα1β2 heterodimer with its cognate receptor LTβR to induce broad effects on FDC maintenance, promoting a favourable microenvironment promoting GC reactions on B cells[67–69]. Furthermore, expression of LTα in the meninges causes *de novo* ectopic lymphoid tissue formation and neurodegeneration[70]. Our data so far indicates that the murine meninges develop ectopic lymphoid aggregates that display many features of LTβ-driven lymphoid tissue formation, including the presence of FDCs like structures, T_{FH} T cells, and GC-like B cells with evidence of somatic hypermutation. Thus, we hypothesised that LTβ-signalling plays a similar role in the formation of meningeal lymphoid aggregates and coordinating the meningeal responses to chronic *T. brucei* infection. *Ltbr,* which encodes for the LTβ receptor, is more widely expressed by cells within the myeloid compartment, endothelial cells, granulocytes, and fibroblasts (**Figure 9A**), indicating that LTβ signalling may occur at multiple levels within the murine meninges. Similarly, LTβ (encoded by *Ltb*) is primarily expressed by the $CD4^+$ T cell clusters and to a lesser extent by cDCs, neutrophils, $CD8^+$ T cells, and B cells (**Figure 9A**). Using flow cytometry, we detected a significant increase in the frequency of $CD4^+$ T cells expressing LTβ (**Figure 9B and 9C**), consistent with their T_{FH} phenotype[27]. Next, we investigated the role of LTβR-signalling in the maintenance of local immunological responses within the meningeal stroma. For this, mice were treated prior and during *T. brucei* infection with a LTβR-Ig fusion protein to prevent the interaction of the ligands LTα1β2 and LIGHT with LTβR (**Figure 9D**). LTβR-Ig treatment resulted in mice unable to control systemic parasitaemia as efficiently as mice treated with an irrelevant antibody or untreated mice (**S5A Figure**), and in a worsening in the clinical scoring (**S5B Figure**), mirroring previous work using *Ltb*$^{-/-}$ mice infected with *T. brucei* in the context of intradermal infections[71]. Furthermore, LTβR-Ig treatment significantly impaired the induction of meningeal FDCs, including the formation of perivascular FDC-B cell clusters (**Figure 9E to 9G**), consistent with previous reports[53,54]. Interestingly, treatment with LTβR-Ig also induced a significant accumulation of meningeal lymphatic endothelial cells compared to naïve controls, which can be attributed to changes in frequencies within other stromal compartments (**Figure 9E and 9F**). Using ELISpot, we observed that LTβR-Ig treatment significantly impaired the expansion of both IgM^+ (**S5C to 5E Figure**) and IgG^+ ASCs, including *T. brucei*- and mouse brain-specific ASCs (**Figure 9H**), consistent with a central role for LTβR-signalling in the formation of B cell follicles and GCs within

secondary lymphoid organs and ectopic lymphoid tissues[53,54,67,71]. Together, these data demonstrate that LTβR signalling is required for stromal responses and B cell accumulation and maturation in the meninges during infection with *T. brucei*, further highlighting that the meninges depend on classical lymphoid tissue-associated signalling pathways to coordinate local immune responses to infections. LTβ receptor (LTβR) signalling is critical for the formation, induction, and maintenance of lymphoid tissues under homeostasis and disease[68,69]. This process requires the interaction between $LT\alpha_1\beta_2$ heterodimer with its cognate receptor LTβR to induce broad effects on FDC differentiation and maintenance, promoting a favourable microenvironment promoting GC reactions on B cells[68,69]. Furthermore, expression of LTα in the meninges causes *de novo* ectopic lymphoid tissue formation and neurodegeneration[70]. Our data so far indicates that the murine meninges develop ectopic lymphoid aggregates that display many features of LTβ-driven lymphoid tissue, including the presence of FDCs, T_{FH} cells, and GC-like B cells with evidence of somatic hypermutation. Thus, we hypothesised that LTβR-signalling plays a similar role in the formation of meningeal lymphoid aggregates and the coordination of the meningeal responses to chronic *T. brucei* infection. *Ltbr,* which encodes for the LTβR, is more widely expressed by cells within the myeloid compartment, endothelial cells, granulocytes, and fibroblasts (**Figure 9A**), indicating that LTβR signalling may occur at multiple levels within the murine meninges. Similarly, LTβ (encoded by *Ltb*) is primarily expressed by the $CD4^+$ T cell clusters and to a lesser extent by cDCs, neutrophils, $CD8^+$ T cells, and B cells (**Figure 9A**). Using flow cytometry, we detected a significant increase in the frequency of $CD4^+$ T cells expressing LTβ (**Figure 9B and 9C**), consistent with their T_{FH} phenotype[27]. Next, we investigated the role of LTβR-signalling in the maintenance of local immunological responses within the meningeal stroma. For this, mice were treated prior and during *T. brucei* infection with a LTβR-Ig fusion protein to prevent the interaction of the ligands $LT\alpha_1\beta_2$ and TNFSF14/LIGHT with LTβR (**Figure 9D**). Mice treated with LTβR-Ig were unable to control systemic parasitaemia as efficiently as mice treated with an irrelevant antibody or untreated mice (**S6A Figure**), and in a worsening in the clinical scoring (**S6B Figure**), mirroring previous work using *Ltb*$^{-/-}$ mice infected with *T. brucei*[71]. Furthermore, LTβR-Ig treatment significantly impaired the induction of meningeal FDCs, including the formation of perivascular FDC-B cell clusters (**Figure 9E to 9G**), consistent with previous reports[53,54].

Because the lack of organised perivascular follicular aggregates could result in poor local affinity maturation and production of autoreactive antibodies, we next examine whether LTBR-Ig treatment impacts mouse brain-reactive IgM^+ and IgG^+ ASCs in the murine meninges. Using ELISpot, we observed that LTβR-Ig treatment significantly impaired the expansion of both IgM^+ (**S6C to 6E Figure**) and IgG^+ ASCs, including *T. brucei*- and mouse brain-specific ASCs (**Figure 9H**), consistent with a central role for LTβR-signalling in the formation of B cell follicles and GCs within secondary lymphoid organs and ectopic lymphoid tissues[53,54,71]. Interestingly, in treatment with LTBR-Ig recued the demyelination observed in response to infection, in particular in the cortex (S6F Figure), further highlighting an association between the formation of ectopic lymphoid aggregates in the meninges and cortical demyelination during chronic infection. Together, these data demonstrate that LTβR signalling is required for stromal responses and B cell accumulation and maturation in the meninges during infection with *T. brucei*, further highlighting that the meninges depend on classical lymphoid tissue-associated signalling pathways to coordinate local immune responses to infections.

Discussion

Here, we set out to characterise the local immune responses taking place within the murine meninges in response to chronic infection with *T. brucei*. Our data demonstrate that the murine meninges are dynamic structures able to support a wide range of immune responses that are triggered upon infection with *T. brucei*, resulting in the acquisition of ectopic lymphoid tissue-like signatures including the development of FDCs-like, T_{FH} cells, and GC-like B cells undergoing class switching. We also showed that during *T. brucei* infection, the murine meninges also harbour a distinctive population of autoreactive B cells that generate IgG^+ antibodies able to bind parasite and murine brain antigens. Furthermore, we demonstrated that the rearrangement of the meningeal stroma, as well as the accumulation of autoreactive B cells, depended upon LTβR signalling, consistent with its lymphoid tissue properties. Lastly, we demonstrated the presence of IgG^+ antibodies in the CSF of 2nd stage gambiense HAT patients (when the parasites accumulate in the meninges and CNS) able to recognise human brain lysates, indicating that the observations using experimental infections are likely to be conserved in humans.

Focussing on the stroma, we identified several populations of meningeal fibroblasts, mostly derived from the dura mater layer of the meninges that express *bona fide*

markers of mesenchymal precursor cells (*Ly6a*$^+$). Furthermore, using pseudotemporal inferences we were able to identify a distinct *Ly6a*$^+$ *Aldh1a2*$^+$ fibroblast precursor population that expressed high levels of *Ccl19* and *Cxcl13*. Interestingly, this population of meningeal fibroblasts shares many transcriptional features with omental *Aldh1a2*$^+$ FRCs that are known to play a critical role in modulating lymphocyte recruitment and local immune responses in the peritoneum[51]. It is tempting to speculate that there exist a pre-defined populations of fibroblasts with precursor capacity (e.g., Ly6a/Sca1$^+$) in several body cavities that are, including the meninges, able to quickly sense and adapt to inflammatory responses to coordinate local immune responses efficiently. In this context, it is plausible that the population of lymphoid stromal cells residing in the dura layer of the meninges sense the presence of *T. brucei* (e.g., *via* TLR or cytokine signalling) to promote local immunological responses, as recently proposed[72]. We propose that these populations meningeal *Ly6a*$^+$ fibroblast precursors could adapt to chronic inflammatory conditions, resulting in the development of stromal structures required to sustain long-lasting immunological responses *in situ*, including FRC- and FDC-like cells, as well as *de novo* angiogenesis. These observations are consistent with the suggestion that chronic neuroinflammation results in lymphangionesis in the CNS[56]. All of these populations are participated in changes in the ECM during infection, including collagen and proteoglycan deposition and regulation of the ECM, highlighting the extensive ECM remodelling taking place in the meninges during chronic infection. The ontogeny of the meningeal FDC-like cells that we detected under chronic infection with *T. brucei*, and whether they play an active role in the neuroinflammatory process in this infection setting[73] requires further examination. Nevertheless, to our knowledge, this is the first report characterising the dynamics of meningeal fibroblasts to chronic infections with a protozoan parasite, which have important implications for understanding how dynamic and adaptable the meningeal stroma is under chronic inflammatory processes.

Additionally, we identified that meningeal mononuclear phagocytes play critical roles in modulating B cell chemotaxis, and antigen presentation to CD4$^+$ T cells. Consistent with recent studies characterising the dynamics of myeloid cells within the brain borders in response to *T. brucei* infection[9,10], we identified several subsets of mononuclear phagocytes and conventional DCs that play a wide range of roles, from inflammatory responses to chemotaxis and antigenic presentation. Overall, all these myeloid subsets might offer a first line of defence against incoming parasites, and together with the

meningeal stroma, might promote the recruitment and activation of adaptive immune cells required to support an efficient local immune response. It also remains to be determined whether the lymphatic structures present within the meninges play an active role in the induction of ectopic lymphoid tissues during chronic *T. brucei*.

We also detected an accumulation of autoreactive B cells able to produce high affinity antibodies against both *T. brucei* and the mouse brain, resembling the pathology observed under autoimmune neurological disorders including MS[74]. Previous work has demonstrated not only the presence of autoreactive antibodies in HAT patients and during experimental infections[75–79], some of which are able to recognise a wide variety of heat shock proteins and ribosomal proteins[75,77] that might be evolutionarily conserved between parasites and host. However, the local generation of autoreactive B cells in the murine meninges able to recognise murine brain lysates in response to chronic infection with *T. brucei* has not been reported before. These observations indicate that the local immunological responses in the meninges could result in the (uncontrolled) production of autoreactive antibodies, explaining their presence in the CSF of 2nd stage *gambiense* HAT patients as shown in this study. Nevertheless, the mechanisms resulting in the development of local autoantibodies remains to be determined.

Based on our dataset and *in vivo* experimental approaches, we conclude that this process relies of LTβR-signalling signalling resulting in the expansion of meningeal FDC-like fibroblasts, and potentially aided by the local development of T_{FH} $CD4^+$ T cells expressing high levels of *Il21* and *Ltβ*, critical to promote GC-like reactions and antibody affinity maturation. In this context, our data demonstrate that chronic meningeal inflammation leads to the formation of B cell-FDC-like cells-T cell aggregates, resembling those within the B cell follicle in lymph nodes and spleen but lacking their typical microarchitecture, to sustain the production of high affinity antibodies locally. It is important to note that the majority of the cells within the B cell compartment were assigned as IgM^+ and IgG^+ plasma cells as shown before[2,41,46,80,81], although their nature (IgA^+ vs IgM^+ or IgG^+) differs slightly from previous elegant work describing the diversity of meningeal B cells compartment during fungal infection[46]. Interestingly, in an experimental autoimmune encephalomyelitis (EAE) model, the frequency of *Igha*$^+$ B cells found in the homeostatic dura matter decreased significantly followed by a significant expansion of *Ighm* and *Ighg* expression in B cells during inflammation[80], in a

process similar to the results presented in this study. These differences might be attributed to technical differences between studies (e.g., depth of coverage) or biological differences due to intrinsic differences between disease conditions. It is important to note that, in addition to the autoreactive IgG^+ ASCs residing in the meninges and identified by ELISpot, vascular leakage (allowing the passage of IgG through the blood-brain barrier) reported in this model[82–84] may also contribute to the IgG deposition detected within the brain. However, at present we cannot directly assess the relative contribution of each process separately. Irrespective of the routes by which autoreactive antibodies reach the meningeal barrier and/or brain parenchyma, further work is required to identify whether they arise as a result of molecular mimicry (e.g., shared epitopes between *T. brucei* and mice) or *via* bystander activation (e.g., continues TLR stimulation on B cells[85,86]). It remains unclear, however, whether the emergence of autoreactive B cells depends upon T cell-mediated responses (antigen-specific) or whether it results from T cell-independent processes (e.g., polyclonal activation, antigen-independent). In the context of T cell-dependent responses, future work is required to determine the nature of the antigens driving such specific responses, as well as the precise ontogeny of T_{FH} T cells (e.g., derived from T_H17 T cells as recently proposed[87]) to the generation of high affinity autoreactive antibodies in the context of chronic infections remains to be delineated in more detail. Irrespective of the routes by which autoreactive antibodies reach the meningeal barrier and/or brain parenchyma, future work is require to determine whether these arise as a result of molecular mimicry (e.g., shared epitopes between *T. brucei* and mice) or *via* bystander activation (e.g., continues TLR stimulation on B cells[85,86]).

The histological features related to antibody deposition in the meningeal and cortical spaces during chronic *T. brucei* infection is associated with cortical and white matter demyelination, which are reminiscent of the histopathological features observed in MS and other neurological autoimmune disorders[88–90]. However, it is unclear whether the cortical pathology observed in our infection model results in primary (B cells generating antibodies against myelin) or secondary demyelination (triggered by neuronal death). Importantly, *Aid*$^{-/-}$ mice in which B cells are unable to undergo affinity maturation are better at controlling *T. brucei* infections due to an increased in circulating (low affinity) IgM, suggesting that class-switching might indeed be a process unfavourable for the host[91]. Based on our data, local B cell affinity maturation and class-switching results in autoimmunity. In this scenario, it is tempting to speculate that most of the

neuropathological features associated with chronic *T. brucei* infection could indeed derive from a disruption in peripheral tolerance resulting in maladaptive antibody responses, as recently demonstrated in variable immune deficiency patients with autoimmune manifestations[92]. Further studies are required to determine the type of antigens detected by the autoreactive antibodies generated in the meninges, and to determine whether they share epitopes with *T. brucei* antigens due to molecular mimicry, as reported for EBV-induced MS[74]. Similarly, it is important to determine if B cell depletion strategies (e.g., B cell depletion approaches[93,94], including treatment with anti-CD20 treatment[95]) or chemotherapy interventions to treat the infection ameliorate disease progression, meningeal inflammation, and cortical pathology during chronic *T. brucei* infection, similar to MS[94].

Together, our data provide a novel perspective for understanding the cellular and molecular mediators that lead to the development of autoimmunity during chronic *T. brucei* infection. Furthermore, our results support the notion that the meningeal spaces are dynamic structures able to support a wide range of immunological responses, including those resulting in pathological outcomes such as autoreactive antibody deposition at the brain borders. In this context, we propose that experimental infections with African trypanosomes can be exploited to address basic questions regarding infection-induced autoimmunity and brain pathology, which could be leveraged for the treatment of complex neurological disorders of unknown aetiology such as MS in addition to the meningoencephalitic stage of sleeping sickness.

Funding and acknowledgments.

We thank Julie Galbraith and Pawel Herzyk (Glasgow Polyomics, University of Glasgow) for their technical support with library preparation and sequencing, and the technical staff at the University of Glasgow Biological Services for their assistance in maintaining optimal husbandry conditions and comfort for the animals used in this study. Similarly, we would like to thank the histopathology unit at the University of Glasgow veterinary school (In particular Frazer Bell and Lynn Stevenson) for their technical assistance with sample processing and preparation. We also thanks Professor Wendy Bailey (Liverpool School of Tropical Medicine, UK) for providing CSF samples from gambiense HAT patients from North Uganda. The authors would also like to thank the III Flow cytometry facility for their support with flow cytometry analysis, Dr. Gareth Howell (university of Manchester) for technical support with the mass cytometry

experiments, and Dr. Chiara Pirillo (Beatson Institute) for technical assistance with the ELISpot assay. This work was funded by a Sir Henry Wellcome postdoctoral fellowship (221640/Z/20/Z to JFQ). AML is a Wellcome Trust Senior Research fellow (209511/Z/17/Z). PC and MCS are supported by a Wellcome Trust Senior Research fellowship (209511/Z/17/Z) awarded to AML. NAM is supported by project Institute Strategic Programme Grant funding from the BBSRC (BBS/E/D/20231762, BBS/E/D/20002174 and BB/X010937/1). The authors declare that the research was conducted in the absence of any commercial or financial relationships that could be construed as a potential conflict of interest.

Author contributions

Conceptualisation: JFQ, NAM. **Methodology:** JFQ, MCS, LKD, PC, JO, GM, MAS. **Sample collection in the field:** NRKS, DMN. **Formal analysis**: JFQ, MCS, PC, MH. **Writing – original draft:** JFQ**. Writing – reviewing and editing:** JFQ, MCS, LKD, GM, NAM, AML. **Funding acquisition:** JFQ. All authors approved the current version of this manuscript. The authors declare that they have no competing interests, commercial or otherwise. Correspondence and requests for materials should be addressed to Juan F. Quintana (juan.quintana@glasgow.ac.uk).

Figures

Figure 1. CyTOF confirms the expansion of innate and adaptive immune cells in the murine meninges during chronic *T. brucei* infection.

A) Overview of the experimental approach applied in this work. An anti-CD45-PE antibody was injected *i.v.* prior to cull, followed by magnetic sorting using anti-PE antibodies to obtain a fraction of resident meningeal cells that were used as input for single cell transcriptomics using the 10X Chromium platform. **B)** Uniform manifold approximation and projection (UMAP) visualisation of the CyTOF immunophenotyping in murine meninges from naïve and animals at 30dpi. The UMAP plot represents pooled data from n = 5-6 mice/group. **C)** Normalised protein expression level of markers used to define T cells and NK cells (TCRβ, TCRγδ, NK1.1), B cells (CD19, B220, IgM), and myeloid cells (CD11b, Ly6G/C, and CD11c). **D)** Quantification of $CD45^+$ cells in the murine meninges at 30dpi (n = 5-6 mice/group). T student test: a p value < 0.05 is considered significant. **E)** Unsupervised cell annotation from CyTOF data using a

combination of several marker genes. The expression level is normalised to the average of the expression within the group. **F)** Quantification of the different populations of immune cells in the naïve and infected murine meninges (*n* = 5-6 mice/group). T student test: a *p* value < 0.05 is considered significant. The data in all panels is expressed as mean ±SD. Data points indicate biological replicates for each panel.

Figure 2. Single cell atlas of the murine meninges during chronic *T. brucei* infection.

A) A total of 20,427 high-quality cells were used for dimensionality reduction, resulting in uniform manifold approximation and projection (UMAP) for the single cell transcriptome profiling. **B)** Dotplot representing the expression levels of top marker genes used to catalogue the diversity of cell types in our single cell dataset. **C)** Frequency of the different cell types detected in the murine meninges analysed in this study.

Figure 3. The meningeal stromal compartment acquires lymphoid-like properties and provide cues for immune cell recruitment during chronic *T. brucei* infection

A) Uniform manifold approximation and projection (UMAP) of 2,088 high-quality cells within the fibroblast clusters were re-analysed to identify a total eight subclusters. **B)** Dot plot representing the expression levels of marker genes previously reported to be enriched in fibroblasts from different meningeal layers, including dura mater, pia mater, and arachnoid mater. **C)** Dot Plot representing the expression levels of top marker genes used to catalogue the diversity of cell types in our single cell dataset. **D)** Frequency plot the different fibroblast clusters detected in the murine meninges in naïve (*n* = 2) and infected. (*n* = 2) samples. **E)** Representative flow cytometry analysis of meningeal stromal cells from naïve and infected meningeal preparations (left panel), and the corresponding quantification **(F)**. A *p* value < 0.05 is considered significant. FRC, fibroblast reticular cells; LECs, lymphatic endothelial cells; BECs, blood endothelial cells; FDCs, follicular dendritic cells. **G)** Module scoring for genes typically associated with lymphoid tissues. **H)** Violin plot depicting the expression of two chemokines associated with lymphoid tissues such as *Ccl19* and *Cxcl13*. **I)** Single molecule fluorescent *in situ* hybridisation (smFISH) demonstrating the presence of *Pdpn*+ cells also expressing *Cxcl13* in the dura mater of the meninges of infected mice. DAPI is included as a nuclear marker. The skull bone, the bone marrow (BM), and the meninges are indicated. Scale bar, 100 μm.

Figure 4. Pseudotemporal trajectory inference for the meningeal fibroblast responses to chronic *T. brucei* infection.

A) Uniform manifold approximation and projection (UMAP) representation of the pseudotemporal reconstruction for the cellular trajectory profiles within the fibroblast subsets, including the root node. The colour of each point in the UMAP represents advancements in the linear trajectory, with darker colours representing "early" transcriptional events coinciding with naïve samples, and lighter colours representing "late" events, coinciding with infected samples. **B)** The line represents the pseudotemporal trajectory inferred by Monocle3 in relation to all the various fibroblast transcriptional clusters. **C)** Expression profile of selected genes depicting those whose expression arise early in the trajectory (left panel) or late in the trajectory (right panel). **D) Top panel:** Expression level of *Cr1l*, which encodes for CD35 used to label FDCs. **Bottom panel:** Representative immunofluorescence analysis of whole mount meningeal preparation using CD21/CD35 to label FDCs, in naïve specimens or at 30 days post-infection. Scale bar = 100 μm. **E) Top panel:** Expression level of *Col6a3*, the antigen recognised by the ER-TR7 antibody; **bottom panel:** Representative immunofluorescence analysis of whole mount meningeal preparation using ER-TR7 antibody, labelling reticular fibroblasts, in naïve or at 30 days post-infection. An inset for the infected sample is also indicated. Scale bar = 100 μm, or 30 μm for the inset.

Figure 5. Heterogeneity of meningeal mononuclear phagocytes during chronic T. brucei infection.

A) Uniform manifold approximation and projection (UMAP) of 1,742 high-quality B cells from naïve (n = 54 cells) and infected meninges (n = 10,706 cells). **B)** Expression level of top genes defining different populations of meningeal mononuclear phagocytes. **C)** Frequency plot depicting the relative abundance of the two B cell subclusters identified in the murine meninges during *T. brucei* infection. **D)** Cell-cell interaction network via MCH-II signalling axis. **E)** Violin plot depicting the expression level of *H2-D1* and *H2-Ab1*, two of the most upregulated MHC-II associated genes within the myeloid compartment. **F)** Representative flow cytometry analysis of meningeal $CD11b^+$ $MHC\text{-}II^+$ mononuclear phagocytes from naïve animals (left) and after 30 days post-infection (right). **G)** Quantification of $CD11b^+$ $MHC\text{-}II^+$ mononuclear phagocytes from (F). **H)** Cell-cell interaction network *via Cxcl* signalling axis.

Figure 6. Accumulation of T_{FH} $CD4^+$ T cells in the meninges during chronic *T. brucei* infection

A) Uniform manifold approximation and projection (UMAP) of 1,742 high-quality T cells from naïve (n = 147 cells) and infected meninges (n = 2,691 cells). **B)** Dot plot depicting the expression level of genes associated with T_{FH} responses (e.g., *Pdcd1, Icos, Stat3, Il21*). The dot size corresponds to the proportion of cells expressing the marker genes, whereas the colour indicates the level of expression. **C)** Flow cytometry analysis to determine TCR engagement in $CD4^+$ (top panel) and $CD8^+$ (bottom panel) T cells *in situ* in the meninges during chronic infection with *T. brucei* using the $Nur77^{GFP}$ reporter mouse line. **D)** Quantification of the flow cytometry data from the ex vivo stimulation assay in (C). A *p* value < 0.05 is considered significant. **E)** *Ex vivo* T cell activation from naïve and infected murine meninges to measure the expression of PD-1 and IL-21. Unstimulated controls are also included. **F)** Quantification of the flow cytometry data from the *ex vivo* stimulation assay in (E). A *p* value < 0.05 is considered significant.

Figure 7. The murine meninges contain class-switched B cells in proximity to FDC-like cells.

A) Dotplot representing the expression level of top marker genes for the meningeal B cell clusters, including *bona fide* markers of plasma cells (*Jchain, Prdm1, Sdc1, Xbp1, Ighm)* as well as replication and class switching *(Ighg2b, Ighg2c, Ighg3, Pcna, Mki67, Ube2c, Aicda*), and DNA damage and repair (*Apex2, Ung, Exo1, Msh6, Poldb*). **B)** Flow cytometry analysis to quantify the IgG^+ B cells from meningeal preparations at 30dpi or naïve controls (*n* = 4 mice/group). A *p* value < 0.05 is considered significant. **C)** Quantification of the flow cytometry data from (C). A *p* value < 0.05 is considered significant. **D)** Flow cytometry analysis to determine BCR engagement on meningeal B cells *in situ* during chronic infection with *T. brucei* using the $Nur77^{GFP}$ reporter mouse line. **E)** Quantification of the flow cytometry data from the ex vivo stimulation assay in (D). A *p* value < 0.05 is considered significant. F) Ridgeplot depicting the expression levels of *Cd38, Cxcr4*, and *Cd86*, which have been postulated as markers for dark zone B cells during GC reactions. **G)** Representative imaging analysis of whole-mount meninges from naïve (left) and infected (right) of $CD21/CD35^+$ follicular dendritic cells (green), as well as $CD3d^+$ T cells (red) and $B220^+$ B cells (purple). DAPI was included as nuclear staining. Scale = 50 μm. **H)** Cell-cell communication prediction between meningeal fibroblasts and B cells. The heatmaps represent the predicted ligand activity,

overall expression level, and log fold change in expression in infected compared to naïve fibroblasts for the top 16 ligands predicted to be expressed by meningeal fibroblasts. **I)** Heatmaps representing the bona fide cell-cell interaction between meningeal fibroblasts ("senders") and B cells ("receivers") mediated by ligand-receptor co-expression. The intensity of the colour represents the strength of the interaction.

Figure 8. The murine meninges contain autoreactive IgG$^+$ antibody secreting cells (ASCs) during chronic *T. brucei* infection.

A) Representative ELISpot images depicting mouse brain-specific IgG$^+$ ASCs from naïve and infected murine meninges after 30dpi with *T. brucei*. **B)** Quantification of ELISpot results including total IgG$^+$, *T. brucei*-specific IgG$^+$, and mouse brain-specific IgG$^+$ antibody secreting cells. Wells coated with BSA were included as negative controls. A p value < 0.05 is considered significant. **C)** Immunohistochemistry analysis to determine IgG$^+$ deposition in the mouse brain from naïve (left) and infected (right) mouse brain sagittal sections. The sections were stained with an anti-mouse IgG antibody coupled to HRP to measure the overall distribution of IgG in the brain. The asterisks denote areas of intense IgG deposition in the leptomeningeal space, as well as in the upper layers of the cerebral cortex, exclusively detected in the infected brain. **D)** Serum titters of mouse brain-specific IgM and IgG antibodies in naïve and infected samples as measured by ELISA. The dotted line represents the average of the optical density detected in naïve controls. A *p* value < 0.05 is considered significant. **E)** Immunohistochemistry analysis to determine the presence of circulating brain autoreactive IgG antibodies in serum from naïve (top panels) and infected animals (middle panels) in the mouse brain from naïve (left) and infected (right) mouse coronal brain sections. Staining with the *T. brucei*-specific protein BiP (bottom panels) is also included to highlight accumulation of parasites in the lateral ventricles (arrowheads). **F)** ELISA analysis of human brain-autoreactive IgM and IgG antibodies in cerebrospinal fluid (CSF) from sleeping sickness patients from 1st stage and 2nd stage HAT (CSF dilution 1:400). A *p* value < 0.05 is considered significant. Wells coated with BSA (5µg/ml) were included as controls.

Figure 9. LTβ signalling is critical to sustain FDC-like networks and autoreactive B cells in the murine meninges in response to *T. brucei* infection.

A) Dot plot depicting the expression level of *Ltb*, and its cognate receptors *Traf2* and *Ltbr*. The dot size corresponds to the proportion of cells expressing the marker genes,

whereas the colour indicates the level of expression. **B)** Representative flow cytometry analysis depicting the expression of LTβ in $CD4^+$ T cells in naïve and mice chronically infected with *T. brucei* (30dpi). **C)** Quantification of flow cytometry analysis (n = 4 mice/group). A *p* value < 0.05 is considered significant. **D)** Overview of the experimental approach applied to block LTβ signalling *in vivo* during chronic *T. brucei* infection. **E)** Representative flow cytometry analysis of the murine meningeal stroma in naïve and mice chronically infected with *T. brucei* (30dpi). FDC-like cells were gated from the double $CD45^-$ mesenchymal cells. **F)** Quantification of the different components of the stroma in naïve and infected meningeal preparations (n = 4 mice/group). A *p* value < 0.05 is considered significant. FRC, fibroblast reticular cell; LEC, lymphatic endothelial cell; BEC, blood endothelial cell; DN, double negative. **G)** Representative immunofluorescence analysis of whole mount meningeal preparation labelling $CD138^+$ plasma cells (red) and $CD21/CD35^+$ FDC-like cells (green) in naïve or at 30 days post-infection. Each of the fluorescent channels are shown individually, and DAPI is included as a nuclear staining. Scale bar = 50 μm. **H)** Quantification of ELISpot results including total IgG^+ (left panel), *T. brucei*-specific IgG^+ (middle panel), and mouse brain-specific IgG^+ antibody secreting cells (right panel) in naïve mice, mice treated with an irrelevant IgG2a antibody, and mice treated with LTBR-Ig (*n* = 4 - 9 mice/group). A *p* value < 0.05 is considered significant.

Supplementary figures

Supplementary figure 1. Quality control measurements of the murine single cell CyTOF and transcriptomics dataset. A) Identification of $CD45^+$ cells in the CyTOF murine meninges dataset. B) Uniform manifold approximation and projection (UMAP) of the CyTOF dataset from samples (left panel; BC10-BC15: naïve; BC11-BC20: 30dpi) experimental groups (right panel) after $CD45^+$ cell clustering. Number of Unique molecular identifies (UMIs), genes, mitochondrial reads, and library complexity (Log10 UMIs/gene) before (**C**) and after (**D**) applying filtering parameters. **E)** Clustree output representing the relationship between different cell clusters at various levels of resolution using the function *FindClusters*.

Supplementary figure 2. Gating strategies for flow cytometry analysis. Gating strategy to identification stromal cells (**A**), $CXCR5^+$ $CD4^+$ T cells (**B**), and B cells (C).

Supplementary figure 3. Expression of lymphoid stromal cells marker genes within the dura fibroblasts. A) Left: Expression level of Marker genes typically associated with fibroblast reticular cells (FRCs). **Right:** Expression level of genes encoding for secreted factors resealed by FRCs. **B)** Marker genes moderately (left) or lowly (right) expressed typically associated with B zone reticular cells (BRC). **C)** Broad classification of the various fibroblasts clusters as FRC- or BRC-like clusters based on the marker genes shown in (A) and (B). In all cases, the size of the dot represents the proportion of cells expressing the markers indicated in each plot. **D)** Feature plots depicting the results from module scoring of the different categories within the MatrisomeDB including collagen and proteoglycan production and deposition, extracellular matrix regulators, and secreted factors.

Supplementary figure 4. Meningeal lymphoid-like aggregates in response to *T. brucei* infection. Additional imaging analysis of whole-mount meninges from naïve (left) and infected (right) of CD21/CD35$^+$ follicular dendritic cells (green), as well as CD3d$^+$ T cells (red) and B220$^+$ B cells (purple). The data correspond to data obtained from two independent meningeal preparations; Replicate 1 and 2 shown in top and bottom panels, respectively. DAPI was included as nuclear staining. Scale = 100 µm.

Supplementary figure 5. Chronic *T. brucei* infection induces demyelination in the CNS. A) Left: Representative ELISpot images depicting mouse brain-specific IgG$^+$ ASCs from naïve and infected murine meninges and splenocytes after 30dpi with *T. brucei*. **Right:** Quantification of ELISpot results from mouse brain-specific IgG$^+$ ASCs in meningeal preps and splenocytes (n = 4 mice/group). A p value < 0.05 is considered significant. Luxol Fast blue staining to determine myelination in naïve (**B**) and infected (**C**) coronal brain sections. Insets how areas of the cortex (Ctx), internal capsule (IC), and thalamus (Th).

Supplementary figure 6. LTβR signalling blockade results in uncontrolled parasitaemia and IgM$^+$ B cell accumulation in the meninges. Parasitaemia (**A**) and clinical scoring (**B**) of mice treated with an irrelevant IgG2a antibody, or with the LTβR-Ig fusion protein. Mice untreated but infected were also included as controls. Representative ELISpot results for meningeal IgM$^+$ (**C**) and IgG$^+$ (**D**) antibody secreting cells (ASCs), including total ASCs (top panel), *T. brucei*-specific ASCs (middle panel), and mouse brain-specific ASCs (bottom panel). The number of spots detected by the automated analysis software is also included. **E**) Quantification of ELISpot results

including total IgM^+ (left panel), *T. brucei*-specific IgM^+ (middle panel), and mouse brain-specific IgM^+ antibody secreting cells (right panel) in naïve mice, mice treated with an irrelevant IgG2a antibody, and mice treated with LTBR-Ig (n = 4 – 9 mice/group). A p value < 0.05 is considered significant. F) Luxol Fast blue staining to determine myelination in sagittal brain sections from infected mice treated with LTBR-Ig or with an irrelevant IgG2a antibody control naïve (2 replicates per condition). Insets how selected cortical areas. Ctx, Cortex. Scale bar: 1mm (whole image) or 50 μm (insets).

Supplementary Tables

Table S1. Quality control including mean reads per cell and median genes per cell before and after filtering out low quality cell types.

Table S2. Overview of the major cell types detected in the single cell dataset at a resolution of 0.7. The total number of cells per cluster, percentages, and marker genes are also included.

Table S3. Marker genes identified for the cells within the fibroblast clusters obtained after subsetting (resolution = 0.6). The total number of cells per cluster, percentages, and marker genes are also included.

Table S4. Marker genes identified for the cells within the mononuclear phagocytes (MNP) cluster obtained after subsetting (resolution = 0.3). The total number of cells per cluster, percentages, and marker genes are also included.

Table S5. Marker genes identified for the cells within the T cell cluster obtained after subsetting (resolution = 0.7). The total number of cells per cluster, percentages, and marker genes are also included.

Table S6. Metadata associated with the human cerebrospinal fluid samples included for autoantibodies against human brain lysates by ELISA.

Bibliography

1. Jacob, L. *et al.* Conserved meningeal lymphatic drainage circuits in mice and humans. *J. Exp. Med.* **219**, e20220035 (2022).
2. Rustenhoven, J. *et al.* Functional characterization of the dural sinuses as a neuroimmune interface. *Cell* **184**, 1000-1016.e27 (2021).
3. Antila, S. *et al.* Development and plasticity of meningeal lymphatic vessels. *J. Exp. Med.* **214**, 3645–3667 (2017).

4. Rustenhoven, J. *et al.* Age-related alterations in meningeal immunity drive impaired CNS lymphatic drainage. *J. Exp. Med.* **220**, e20221929 (2023).
5. Bolte, A. C. *et al.* The meningeal transcriptional response to traumatic brain injury and aging. *eLife* **12**, e81154 (2023).
6. Ma, T., Wang, F., Xu, S. & Huang, J. H. Meningeal immunity: Structure, function and a potential therapeutic target of neurodegenerative diseases. *Brain. Behav. Immun.* **93**, 264–276 (2021).
7. Merlini, A. *et al.* Distinct roles of the meningeal layers in CNS autoimmunity. *Nat. Neurosci.* **25**, 887–899 (2022).
8. Ampie, L. & McGavern, D. B. Immunological defense of CNS barriers against infections. *Immunity* **55**, 781–799 (2022).
9. Coles, J. A. *et al.* Intravital Imaging of a Massive Lymphocyte Response in the Cortical Dura of Mice after Peripheral Infection by Trypanosomes. *PLoS Negl. Trop. Dis.* **9**, e0003714 (2015).
10. Vlaminck, K. D. *et al.* Differential plasticity and fate of brain-resident and recruited macrophages during the onset and resolution of neuroinflammation. *Immunity* **55**, 2085-2102.e9 (2022).
11. Coles, J. A., Stewart-Hutchinson, P. J., Myburgh, E. & Brewer, J. M. The mouse cortical meninges are the site of immune responses to many different pathogens, and are accessible to intravital imaging. *Methods San Diego Calif* **127**, 53–61 (2017).
12. Rodgers, J., Bradley, B. & Kennedy, P. G. E. Delineating neuroinflammation, parasite CNS invasion, and blood-brain barrier dysfunction in an experimental murine model of human African trypanosomiasis. *Methods San Diego Calif* **127**, 79–87 (2017).
13. Quintana, J. F. *et al.* Single cell and spatial transcriptomic analyses reveal microglia-plasma cell crosstalk in the brain during Trypanosoma brucei infection. *Nat. Commun.* **13**, 5752 (2022).
14. Blum, J., Schmid, C. & Burri, C. Clinical aspects of 2541 patients with second stage human African trypanosomiasis. *Acta Trop.* **97**, 55–64 (2006).
15. Kazumba, L. M., Kaka, J.-C. T., Ngoyi, D. M. & Tshala-Katumbay, D. Mortality trends and risk factors in advanced stage-2 Human African Trypanosomiasis: A critical appraisal of 23 years of experience in the Democratic Republic of Congo. *PLoS Negl. Trop. Dis.* **12**, e0006504 (2018).

16. Mudji, J. *et al.* Gambiense Human African Trypanosomiasis Sequelae after Treatment: A Follow-Up Study 12 Years after Treatment. *Trop. Med. Infect. Dis.* **5**, 10 (2020).
17. Rijo-Ferreira, F. *et al.* Sleeping Sickness Disrupts the Sleep-Regulating Adenosine System. *J. Neurosci. Off. J. Soc. Neurosci.* **40**, 9306–9316 (2020).
18. Rijo-Ferreira, F. *et al.* Sleeping sickness is a circadian disorder. *Nat. Commun.* **9**, 62 (2018).
19. Lundkvist, G. B., Hill, R. H. & Kristensson, K. Disruption of Circadian Rhythms in Synaptic Activity of the Suprachiasmatic Nuclei by African Trypanosomes and Cytokines. *Neurobiol. Dis.* **11**, 20–27 (2002).
20. Cornford, E. M., Freeman, B. J. & MacInnis, A. J. Physiological Relationships and Circadian Periodicities in Rodent Trypanosomes. *Trans. R. Soc. Trop. Med. Hyg.* **70**, 238–243 (1976).
21. Manzo, A. *et al.* Systematic microanatomical analysis of CXCL13 and CCL21 in situ production and progressive lymphoid organization in rheumatoid synovitis. *Eur. J. Immunol.* **35**, 1347–1359 (2005).
22. Chang, A. *et al.* In situ B cell-mediated immune responses and tubulointerstitial inflammation in human lupus nephritis. *J. Immunol. Baltim. Md 1950* **186**, 1849–1860 (2011).
23. Fridman, W. H. *et al.* B cells and tertiary lymphoid structures as determinants of tumour immune contexture and clinical outcome. *Nat. Rev. Clin. Oncol.* **19**, 441–457 (2022).
24. Pitzalis, C., Jones, G. W., Bombardieri, M. & Jones, S. A. Ectopic lymphoid-like structures in infection, cancer and autoimmunity. *Nat. Rev. Immunol.* **14**, 447–462 (2014).
25. Stock, A. D. *et al.* Tertiary lymphoid structures in the choroid plexus in neuropsychiatric lupus. *JCI Insight* **4**, e124203.
26. Pikor, N. B., Prat, A., Bar-Or, A. & Gommerman, J. L. Meningeal Tertiary Lymphoid Tissues and Multiple Sclerosis: A Gathering Place for Diverse Types of Immune Cells during CNS Autoimmunity. *Front. Immunol.* **6**, (2016).
27. Rodriguez, A. B. *et al.* Immune mechanisms orchestrate tertiary lymphoid structures in tumors via cancer-associated fibroblasts. *Cell Rep.* **36**, 109422 (2021).
28. Ransohoff, R. M. Multiple sclerosis: role of meningeal lymphoid aggregates in progression independent of relapse activity. *Trends Immunol.* **44**, 266–275 (2023).

29. Jalkanen, S. & Salmi, M. Lymphatic endothelial cells of the lymph node. *Nat. Rev. Immunol.* **20**, 566–578 (2020).
30. Krishnamurty, A. T. & Turley, S. J. Lymph node stromal cells: cartographers of the immune system. *Nat. Immunol.* **21**, 369–380 (2020).
31. von Andrian, U. H. & Mempel, T. R. Homing and cellular traffic in lymph nodes. *Nat. Rev. Immunol.* **3**, 867–878 (2003).
32. Phan, T. G., Grigorova, I., Okada, T. & Cyster, J. G. Subcapsular encounter and complement-dependent transport of immune complexes by lymph node B cells. *Nat. Immunol.* **8**, 992–1000 (2007).
33. Da Mesquita, S., Fu, Z. & Kipnis, J. The Meningeal Lymphatic System: A New Player in Neurophysiology. *Neuron* **100**, 375–388 (2018).
34. Louveau, A. *et al.* CNS lymphatic drainage and neuroinflammation are regulated by meningeal lymphatic vasculature. *Nat. Neurosci.* **21**, 1380–1391 (2018).
35. Le Ray, D., Barry, J. D., Easton, C. & Vickerman, K. First tsetse fly transmission of the 'AnTat' serodeme of Trypanosoma brucei. *Ann. Soc. Belg. Med. Trop.* **57**, 369–381 (1977).
36. Herbert, W. J. & Lumsden, W. H. Trypanosoma brucei: a rapid 'matching' method for estimating the host's parasitemia. *Exp. Parasitol.* **40**, 427–431 (1976).
37. Hao, Y. *et al.* Integrated analysis of multimodal single-cell data. *Cell* **184**, 3573-3587.e29 (2021).
38. Hafemeister, C. & Satija, R. Normalization and variance stabilization of single-cell RNA-seq data using regularized negative binomial regression. *Genome Biol.* **20**, 296 (2019).
39. Clustering trees: a visualization for evaluating clusterings at multiple resolutions | GigaScience | Oxford Academic. https://academic.oup.com/gigascience/article/7/7/giy083/5052205.
40. Efremova, M., Vento-Tormo, M., Teichmann, S. A. & Vento-Tormo, R. CellPhoneDB: inferring cell-cell communication from combined expression of multi-subunit ligand-receptor complexes. *Nat. Protoc.* **15**, 1484–1506 (2020).
41. Brioschi, S. *et al.* Heterogeneity of meningeal B cells reveals a lymphopoietic niche at the CNS borders. *Science* **373**, eabf9277 (2021).
42. Shao, X., Taha, I. N., Clauser, K. R., Gao, Y. (Tom) & Naba, A. MatrisomeDB: the ECM-protein knowledge database. *Nucleic Acids Res.* **48**, D1136–D1144 (2020).

43. Intravascular staining for discrimination of vascular and tissue leukocytes | Springer Nature Experiments. https://experiments.springernature.com/articles/10.1038/nprot.2014.005.
44. Manglani, M., Gossa, S. & McGavern, D. B. Leukocyte Isolation from Brain, Spinal Cord, and Meninges for Flow Cytometric Analysis. *Curr. Protoc. Immunol.* **121**, e44 (2018).
45. Browning, J. L. *et al.* Characterization of lymphotoxin-alpha beta complexes on the surface of mouse lymphocytes. *J. Immunol. Baltim. Md 1950* **159**, 3288–3298 (1997).
46. Fitzpatrick, Z. *et al.* Gut-educated IgA plasma cells defend the meningeal venous sinuses. *Nature* **587**, 472–476 (2020).
47. Dorrier, C. E., Jones, H. E., Pintarić, L., Siegenthaler, J. A. & Daneman, R. Emerging roles for CNS fibroblasts in health, injury and disease. *Nat. Rev. Neurosci.* **23**, 23–34 (2022).
48. DeSisto, J. *et al.* Single-Cell Transcriptomic Analyses of the Developing Meninges Reveal Meningeal Fibroblast Diversity and Function. *Dev. Cell* **54**, 43-59.e4 (2020).
49. Jones, H. E. *et al.* Meningeal origins and dynamics of perivascular fibroblast development on the mouse cerebral vasculature. 2023.03.23.533982 Preprint at https://doi.org/10.1101/2023.03.23.533982 (2023).
50. Di Carlo, S. E. & Peduto, L. The perivascular origin of pathological fibroblasts. *J. Clin. Invest.* **128**, 54–63.
51. Aldh1a2+ fibroblastic reticular cells regulate lymphocyte recruitment in omental milky spots | Journal of Experimental Medicine | Rockefeller University Press. https://rupress.org/jem/article/220/5/e20221813/213908/Aldh1a2-fibroblastic-reticular-cells-regulate.
52. Cinti, I. & Denton, A. E. Lymphoid stromal cells—more than just a highway to humoral immunity. *Oxf. Open Immunol.* **2**, iqab011 (2021).
53. Krautler, N. J. *et al.* Follicular Dendritic Cells Emerge from Ubiquitous Perivascular Precursors. *Cell* **150**, 194–206 (2012).
54. McCulloch, L. *et al.* Follicular Dendritic Cell-Specific Prion Protein (PrPc) Expression Alone Is Sufficient to Sustain Prion Infection in the Spleen. *PLOS Pathog.* **7**, e1002402 (2011).
55. Trapnell, C. *et al.* The dynamics and regulators of cell fate decisions are revealed by pseudotemporal ordering of single cells. *Nat. Biotechnol.* **32**, 381–386 (2014).

56. Hsu, M. *et al.* Neuroinflammation-induced lymphangiogenesis near the cribriform plate contributes to drainage of CNS-derived antigens and immune cells. *Nat. Commun.* **10**, 229 (2019).
57. Schiavinato, A., Przyklenk, M., Kobbe, B., Paulsson, M. & Wagener, R. Collagen type VI is the antigen recognized by the ER-TR7 antibody. *Eur. J. Immunol.* **51**, 2345–2347 (2021).
58. Van Hove, H. *et al.* A single-cell atlas of mouse brain macrophages reveals unique transcriptional identities shaped by ontogeny and tissue environment. *Nat. Neurosci.* **22**, 1021–1035 (2019).
59. Moran, A. E. *et al.* T cell receptor signal strength in Treg and iNKT cell development demonstrated by a novel fluorescent reporter mouse. *J. Exp. Med.* **208**, 1279–1289 (2011).
60. Barinov, A. *et al.* Essential role of immobilized chemokine CXCL12 in the regulation of the humoral immune response. *Proc. Natl. Acad. Sci. U. S. A.* **114**, 2319–2324 (2017).
61. Cheng, Q. *et al.* CXCR4–CXCL12 interaction is important for plasma cell homing and survival in NZB/W mice. *Eur. J. Immunol.* **48**, 1020–1029 (2018).
62. Pilzecker, B. & Jacobs, H. Mutating for Good: DNA Damage Responses During Somatic Hypermutation. *Front. Immunol.* **10**, (2019).
63. Mueller, J., Matloubian, M. & Zikherman, J. An in vivo reporter reveals active B cell receptor signaling in the germinal center. *J. Immunol. Baltim. Md 1950* **194**, 2993–2997 (2015).
64. Brooks, J. F. *et al.* Negative feedback by NUR77/Nr4a1 restrains B cell clonal dominance during early T-dependent immune responses. *Cell Rep.* **36**, 109645 (2021).
65. Allen, C. D., Okada, T. & Cyster, J. G. Germinal Center Organization and Cellular Dynamics. *Immunity* **27**, 190–202 (2007).
66. Kang, J.-A., Kim, W.-S. & Park, S.-G. Notch1 is an important mediator for enhancing of B-cell activation and antibody secretion by Notch ligand. *Immunology* **143**, 550–559 (2014).
67. Lymphotoxin-Dependent B Cell-FRC Crosstalk Promotes De Novo Follicle Formation and Antibody Production following Intestinal Helminth Infection - PubMed. https://pubmed.ncbi.nlm.nih.gov/27160906/.

68. Tang, H., Zhu, M., Qiao, J. & Fu, Y.-X. Lymphotoxin signalling in tertiary lymphoid structures and immunotherapy. *Cell. Mol. Immunol.* **14**, 809–818 (2017).
69. Koroleva, E. P., Fu, Y.-X. & Tumanov, A. V. Lymphotoxin in physiology of lymphoid tissues - implication for antiviral defense. *Cytokine* **101**, 39–47 (2018).
70. James Bates, R. E. *et al.* Lymphotoxin-alpha expression in the meninges causes lymphoid tissue formation and neurodegeneration. *Brain* **145**, 4287–4307 (2022).
71. Alfituri, O. A., Bradford, B. M., Paxton, E., Morrison, L. J. & Mabbott, N. A. Influence of the Draining Lymph Nodes and Organized Lymphoid Tissue Microarchitecture on Susceptibility to Intradermal Trypanosoma brucei Infection. *Front. Immunol.* **11**, 1118 (2020).
72. Targeting TLR4 during vaccination boosts MAdCAM-1+ lymphoid stromal cell activation and promotes the aged germinal center response | Science Immunology. https://www.science.org/doi/10.1126/sciimmunol.abk0018.
73. Blockade of VEGFR3 signaling leads to functional impairment of dural lymphatic vessels without affecting autoimmune neuroinflammation | Science Immunology. https://www.science.org/doi/10.1126/sciimmunol.abq0375.
74. Longitudinal analysis reveals high prevalence of Epstein-Barr virus associated with multiple sclerosis | Science. https://www.science.org/doi/10.1126/science.abj8222.
75. Guillaume, M.-P., Hermanus, N., Demulder, A., Servais, G. & Karmali, R. Specific autoantibodies of SLE, such as anti-Ku, anti-ribosome Po and anti-membrane DNA autoantibodies, in a case of human African trypanosomiasis. *Rheumatology* **42**, 1568–1569 (2003).
76. Radwanska, M. *et al.* Antibodies raised against the flagellar pocket fraction of Trypanosoma brucei preferentially recognize HSP60 in cDNA expression library. *Parasite Immunol.* **22**, 639–650 (2000).
77. Radwanska, M. *et al.* Comparative Analysis of Antibody Responses against HSP60, Invariant Surface Glycoprotein 70, and Variant Surface Glycoprotein Reveals a Complex Antigen-Specific Pattern of Immunoglobulin Isotype Switching during Infection by *Trypanosoma brucei*. *Infect. Immun.* **68**, 848–860 (2000).
78. Ayed, Z. *et al.* Detection and Characterization of Autoantibodies Directed against Neurofilament Proteins in Human African Trypanosomiasis. *Am. J. Trop. Med. Hyg.* **57**, 1–6 (1997).

79. Kazyumba, G., Berney, M., Brighouse, G., Cruchaud, A. & Lambert, P. H. Expression of the B cell repertoire and autoantibodies in human African trypanosomiasis. *Clin. Exp. Immunol.* **65**, 10–18 (1986).
80. Schafflick, D. *et al.* Single-cell profiling of CNS border compartment leukocytes reveals that B cells and their progenitors reside in non-diseased meninges. *Nat. Neurosci.* **24**, 1225–1234 (2021).
81. Kovacs, M. A. *et al.* Meningeal lymphatic drainage promotes T cell responses against Toxoplasma gondii but is dispensable for parasite control in the brain. *eLife* **11**, e80775 (2022).
82. De Niz, M. *et al.* Organotypic endothelial adhesion molecules are key for Trypanosoma brucei tropism and virulence. *Cell Rep.* **36**, 109741 (2021).
83. Philip, K. A., Dascombe, M. J., Fraser, P. A. & Pentreath, V. W. Blood-brain barrier damage in experimental African trypanosomiasis. *Ann. Trop. Med. Parasitol.* **88**, 607–616 (1994).
84. Rodgers, J. *et al.* Magnetic resonance imaging to assess blood-brain barrier damage in murine trypanosomiasis. *Am. J. Trop. Med. Hyg.* **84**, 344–350 (2011).
85. Fillatreau, S., Manfroi, B. & Dörner, T. Toll-like receptor signalling in B cells during systemic lupus erythematosus. *Nat. Rev. Rheumatol.* **17**, 98–108 (2021).
86. Hua, Z. & Hou, B. TLR signaling in B-cell development and activation. *Cell. Mol. Immunol.* **10**, 103–106 (2013).
87. Hartlehnert, M. *et al.* Bcl6 controls meningeal Th17–B cell interaction in murine neuroinflammation. *Proc. Natl. Acad. Sci.* **118**, e2023174118 (2021).
88. Lopez, J. A., Denkova, M., Ramanathan, S., Dale, R. C. & Brilot, F. Pathogenesis of autoimmune demyelination: from multiple sclerosis to neuromyelitis optica spectrum disorders and myelin oligodendrocyte glycoprotein antibody-associated disease. *Clin. Transl. Immunol.* **10**, e1316 (2021).
89. Lucchinetti, C. F. *et al.* Inflammatory Cortical Demyelination in Early Multiple Sclerosis. *N. Engl. J. Med.* **365**, 2188–2197 (2011).
90. Cikes, N., Bosnic, D. & Sentic, M. Non-MS autoimmune demyelination. *Clin. Neurol. Neurosurg.* **110**, 905–912 (2008).
91. Nguyen, H. T. T., Guevarra, R. B., Magez, S. & Radwanska, M. Single-cell transcriptome profiling and the use of AID deficient mice reveal that B cell activation combined with antibody class switch recombination and somatic hypermutation do

not benefit the control of experimental trypanosomosis. *PLoS Pathog.* **17**, e1010026 (2021).

92. Friman, V. *et al.* Defective peripheral B cell selection in common variable immune deficiency patients with autoimmune manifestations. *Cell Rep.* **42**, (2023).
93. Magliozzi, R., Marastoni, D. & Calabrese, M. The BAFF / APRIL system as therapeutic target in multiple sclerosis. *Expert Opin. Ther. Targets* **24**, 1135–1145 (2020).
94. Lee, D. S. W., Rojas, O. L. & Gommerman, J. L. B cell depletion therapies in autoimmune disease: advances and mechanistic insights. *Nat. Rev. Drug Discov.* **20**, 179–199 (2021).
95. Florou, D., Katsara, M., Feehan, J., Dardiotis, E. & Apostolopoulos, V. Anti-CD20 Agents for Multiple Sclerosis: Spotlight on Ocrelizumab and Ofatumumab. *Brain Sci.* **10**, 758 (2020).

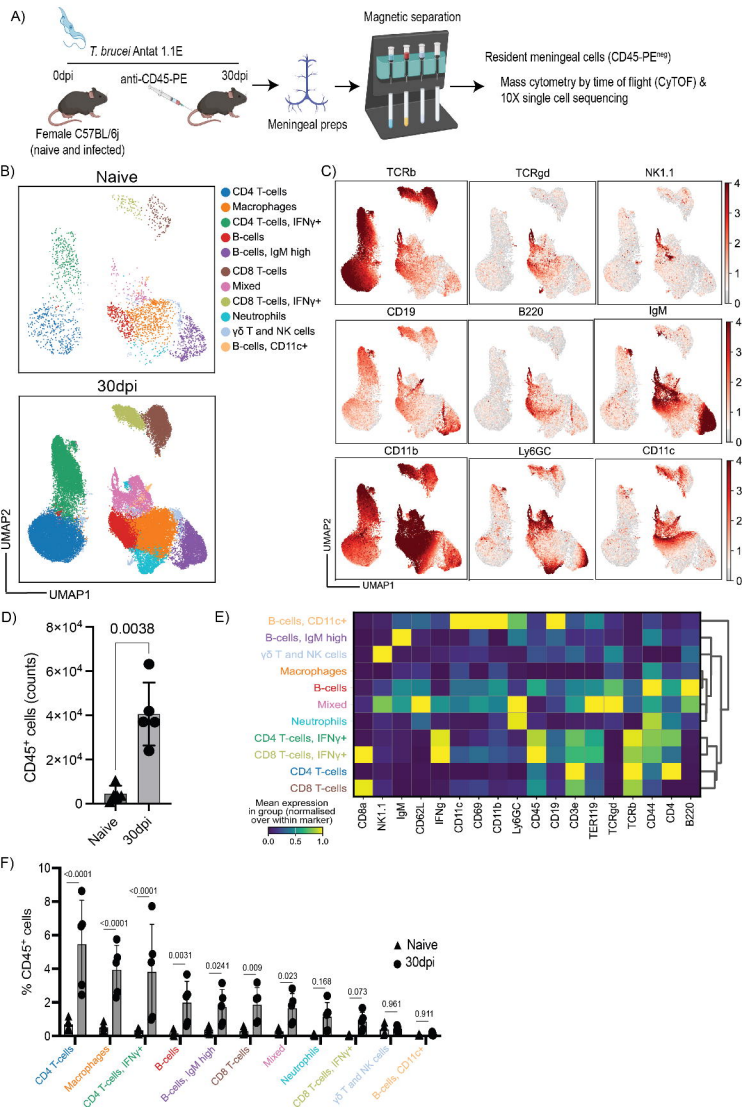
A)
T. brucei Antat 1.1E
0dpi
anti-CD45-PE
30dpi
Female C57BL/6j
(naive and infected)
Meningeal preps
Magnetic separation
Resident meningeal cells (CD45-PE^hsi)
Mass cytometry by time of fiight (CyTOF) &
10X single cell sequencing
B)
Naive
30dpi
UMAP2
UMAP1
CD4 T-cells
Macrophages
CD4 T-cells, IFNγ+
B-cells
B-cells, IgM high
CD8 T-cells
Mixed
CD8 T-cells, IFNγ+
Neutrophils
γδ T and NK cells
B-cells, CD11c+
C)
TCRb
TCRgd
NK1.1
CD19
B220
IgM
CD11b
Ly6GC
CD11c
UMAP2
UMAP1
D)
CD45+ cells (counts)
0.0038
Naive
30dpi
E)
B-cells, CD11c+
B-cells, IgM high
γδ T and NK cells
Macrophages
B-cells
Mixed
Neutrophils
CD4 T-cells, IFNγ+
CD8 T-cells, IFNγ+
CD4 T-cells
CD8 T-cells
CD8a
NK1.1
IgM
CD62L
IFNg
CD11c
CD69
CD11b
Ly6GC
CD45
CD19
CD3e
TER119
TCRgd
TCRb
CD44
CD4
B220
Mean expression in group (normalised over within marker)
F)
% CD45+ cells
Naive
30dpi
<0.0001
<0.0001
<0.0001
0.0031
0.0241
0.009
0.023
0.168
0.073
0.961
0.911
CD4 T-cells
Macrophages
CD4 T-cells, IFNγ+
B-cells
B-cells, IgM high
CD8 T-cells
Mixed
Neutrophils
CD8 T-cells, IFNγ+
γδ T and NK cells
B-cells, CD11c+

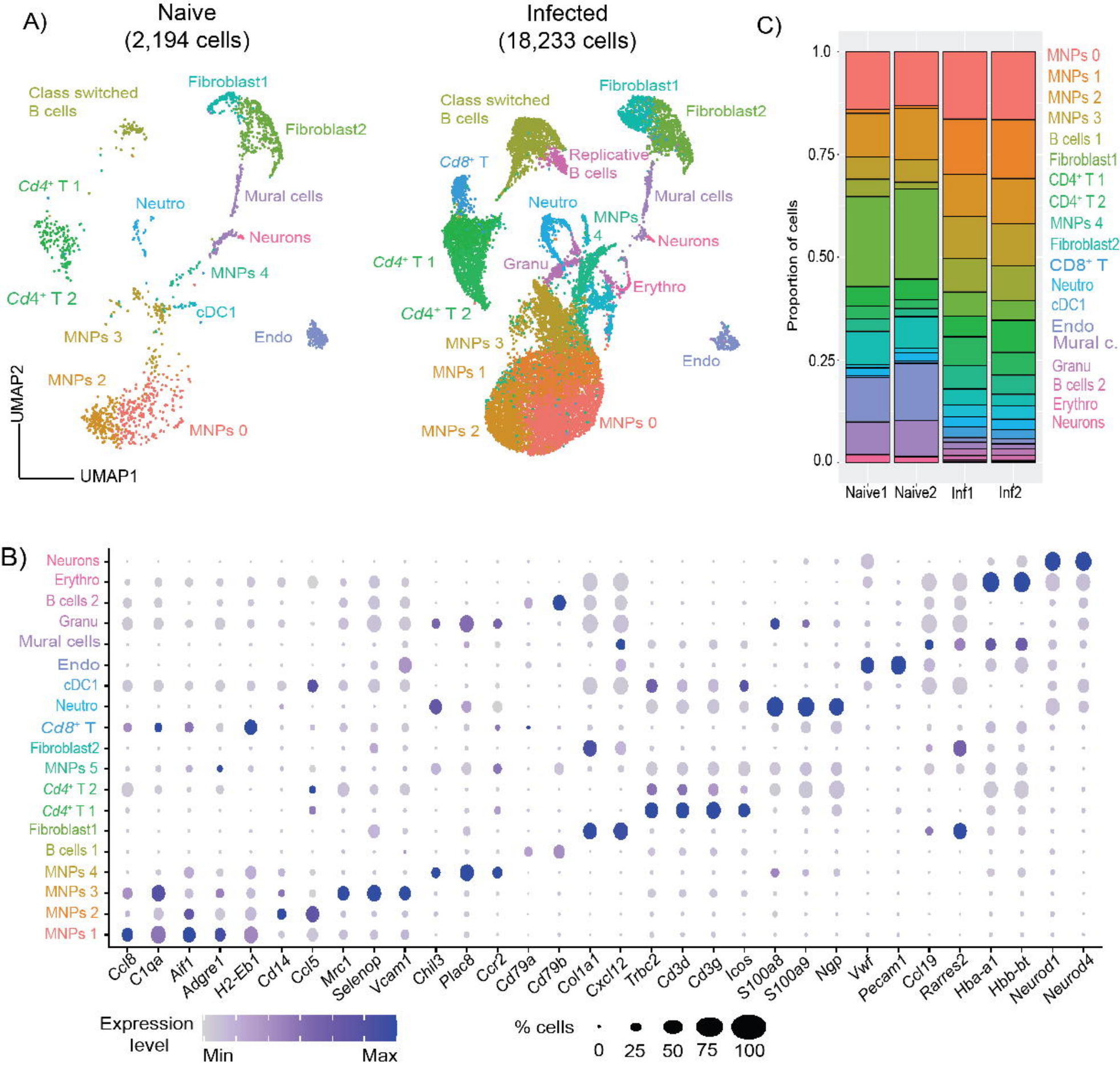
A)
Naive
(2,194 cells)
Infected
(18,233 cells)
Class switched B cells
Fibroblast1
Fibroblast2
Cd4+ T 1
Neutro
Mural cells
Neurons
MNPs 4
Cd4+ T 2
cDC1
MNPs 3
Endo
MNPs 2
MNPs 0
UMAP2
UMAP1
Cd8+ T
Replicative B cells
Granu
Erythro
MNPs 1
C)
Proportion of cells
1.0
0.75
0.50
0.25
0.0
Naive1
Naive2
Inf1
Inf2
MNPs 0
MNPs 1
MNPs 2
MNPs 3
B cells 1
Fibroblast1
CD4+ T 1
CD4+ T 2
MNPs 4
Fibroblast2
CD8+ T
Neutro
cDC1
Endo
Mural c.
Granu
B cells 2
Erythro
Neurons
B)
Neurons
Erythro
B cells 2
Granu
Mural cells
Endo
cDC1
Neutro
Cd8+ T
Fibroblast2
MNPs 5
Cd4+ T 2
Cd4+ T 1
Fibroblast1
B cells 1
MNPs 4
MNPs 3
MNPs 2
MNPs 1
Ccl8
C1qa
Aif1
Adgre1
H2-Eb1
Cd14
Ccl5
Mrc1
Selenop
Vcam1
Chil3
Plac8
Ccr2
Cd79a
Cd79b
Col1a1
Cxcl12
Trbc2
Cd3d
Cd3g
Icos
S100a8
S100a9
Ngp
Vwf
Pecam1
Ccl19
Rarres2
Hba-a1
Hbb-bt
Neurod1
Neurod4
Expression level
Min
Max
% cells
0
25
50
75
100

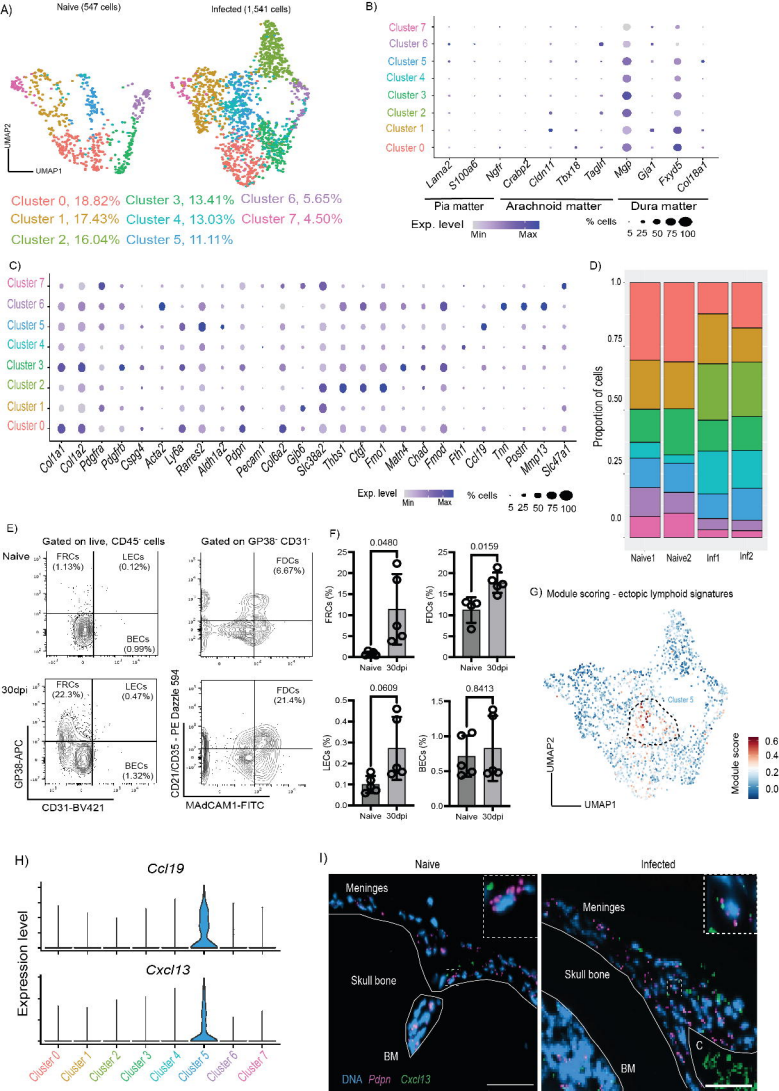
A)
Naive (547 cells)
Infected (1,541 cells)
UMAP2
UMAP1
Cluster 0, 18.82%
Cluster 1, 17.43%
Cluster 2, 16.04%
Cluster 3, 13.41%
Cluster 4, 13.03%
Cluster 5, 11.11%
Cluster 6, 5.65%
Cluster 7, 4.50%
B)
Cluster 7
Cluster 6
Cluster 5
Cluster 4
Cluster 3
Cluster 2
Cluster 1
Cluster 0
Lama2
S100a6
Ngfr
Crabp2
Cldn11
Tbx18
Taglfl
Mgp
Gja1
Fxyd5
Col18a1
Pia matter
Arachnoid matter
Dura matter
Exp. level
Min
Max
% cells
5 25 50 75 100
C)
Cluster 7
Cluster 6
Cluster 5
Cluster 4
Cluster 3
Cluster 2
Cluster 1
Cluster 0
Col1a1
Col1a2
Pdgfra
Pdgfrb
Cspg4
Acta2
Ly6a
Rarres2
Aldh1a2
Pdpn
Pecam1
Col6a2
Gjb6
Slc38a2
Thbs1
Ctgf
Fmo1
Matn4
Chad
Fmod
Fth1
Ccl19
Tnn
Postn
Mmp13
Slc47a1
Exp. level
Min
Max
% cells
5 25 50 75 100
D)
Proportion of cells
1.0
0.75
0.50
0.25
0.0
Naive1
Naive2
Inf1
Inf2
E)
Gated on live, CD45⁻ cells
Gated on GP38⁻ CD31⁻
Naive
FRCs (1.13%)
LECs (0.12%)
BECs (0.99%)
FDCs (6.67%)
30dpi
FRCs (22.3%)
LECs (0.47%)
BECs (1.32%)
FDCs (21.4%)
GP38-APC
CD31-BV421
CD21/CD35 - PE Dazzle 594
MAdCAM1-FITC
F)
0.0480
0.0159
0.0609
0.8413
FRCs (%)
FDCs (%)
LECs (%)
BECs (%)
Naive
30dpi
G) Module scoring - ectopic lymphoid signatures
Cluster 5
UMAP2
UMAP1
Module score
0.6
0.4
0.2
0.0
H)
Ccl19
Cxcl13
Expression level
Cluster 0
Cluster 1
Cluster 2
Cluster 3
Cluster 4
Cluster 5
Cluster 6
Cluster 7
I)
Naive
Infected
Meninges
Skull bone
BM
DNA Pdpn Cxcl13
C

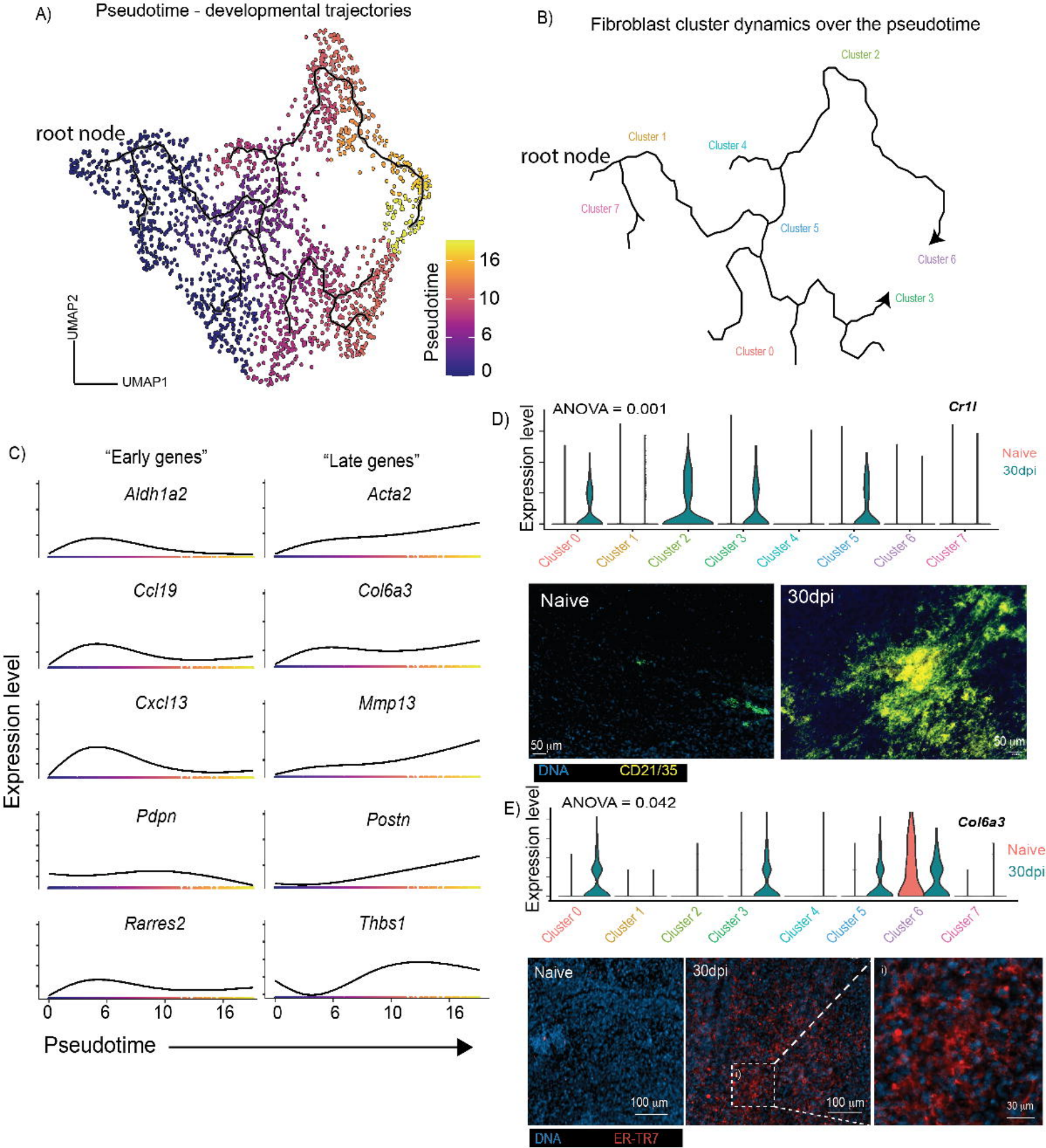
A)
Pseudotime - developmental trajectories
root node
UMAP2
UMAP1
Pseudotime
16
10
6
0
B)
Fibroblast cluster dynamics over the pseudotime
root node
Cluster 2
Cluster 1
Cluster 4
Cluster 7
Cluster 5
Cluster 6
Cluster 3
Cluster 0
C)
"Early genes"
"Late genes"
Aldh1a2
Acta2
Ccl19
Col6a3
Cxcl13
Mmp13
Pdpn
Postn
Rarres2
Thbs1
Expression level
0
6
10
16
Pseudotime
D)
ANOVA = 0.001
Cr1l
Expression level
Naive
30dpi
Cluster 0
Cluster 1
Cluster 2
Cluster 3
Cluster 4
Cluster 5
Cluster 6
Cluster 7
Naive
30dpi
50 µm
50 µm
DNA
CD21/35
E)
ANOVA = 0.042
Col6a3
Expression level
Naive
30dpi
Cluster 0
Cluster 1
Cluster 2
Cluster 3
Cluster 4
Cluster 5
Cluster 6
Cluster 7
Naive
30dpi
i)
100 µm
100 µm
30 µm
DNA
ER-TR7

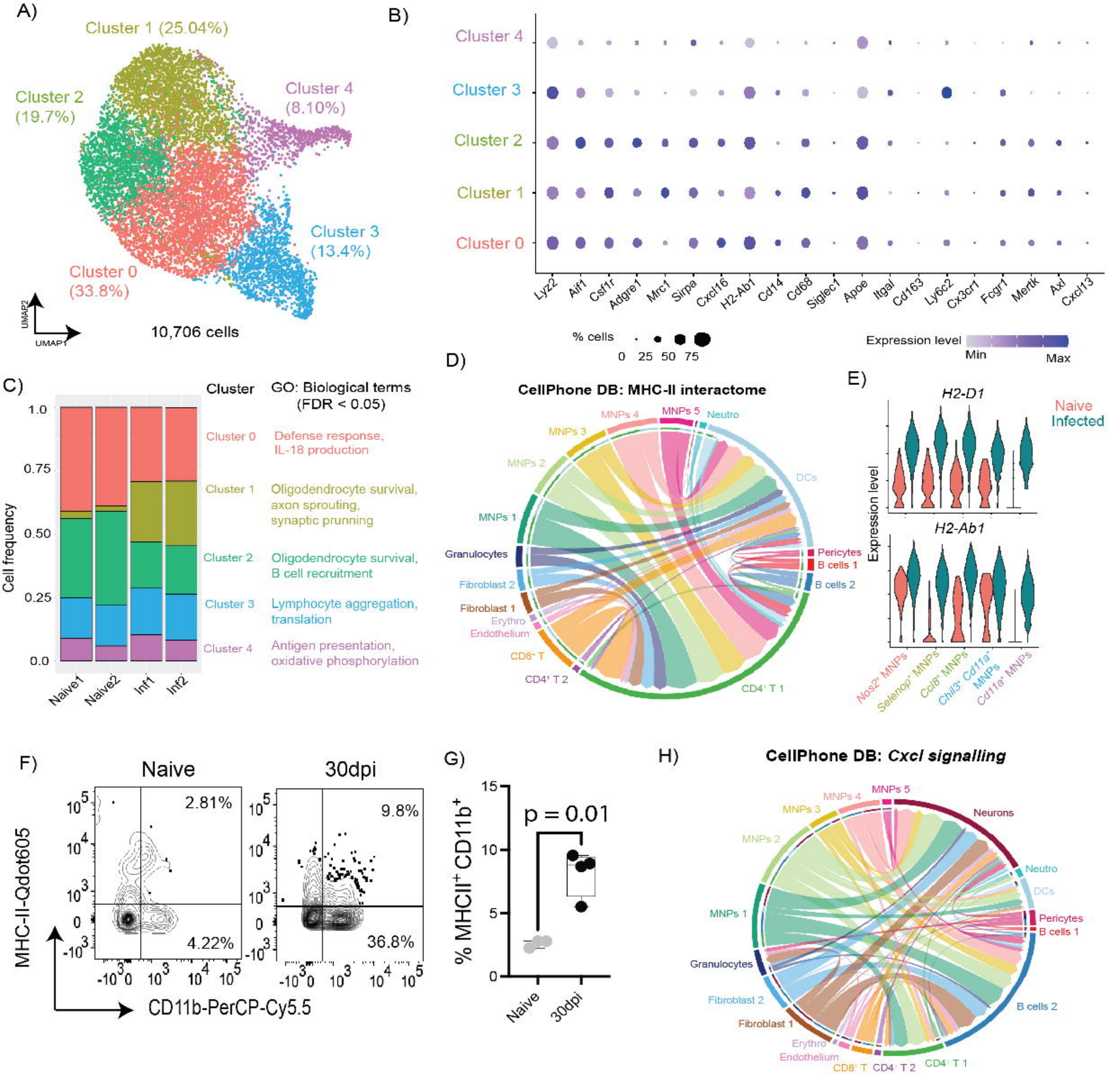
A)
Cluster 1 (25.04%)
Cluster 2 (19.7%)
Cluster 4 (8.10%)
Cluster 3 (13.4%)
Cluster 0 (33.8%)
UMAP2
UMAP1
10,706 cells
B)
Cluster 4
Cluster 3
Cluster 2
Cluster 1
Cluster 0
Lyz2
Aif1
Csf1r
Adgre1
Mrc1
Sirpa
Cxcl16
H2-Ab1
Cd14
Cd68
Siglec1
Apoe
Itgal
Cd163
Ly6c2
Cx3cr1
Fcgr1
Mertk
Axl
Cxcl13
% cells
0 25 50 75
Expression level
Min
Max
C)
Cluster
GO: Biological terms (FDR < 0.05)
Cell frequency
1.0
0.75
0.50
0.25
0.0
Naive1
Naive2
Inf1
Inf2
Cluster 0
Defense response, IL-18 production
Cluster 1
Oligodendrocyte survival, axon sprouting, synaptic prunning
Cluster 2
Oligodendrocyte survival, B cell recruitment
Cluster 3
Lymphocyte aggregation, translation
Cluster 4
Antigen presentation, oxidative phosphorylation
D)
CellPhone DB: MHC-II interactome
MNPs 4
MNPs 5
Neutro
MNPs 3
MNPs 2
DCs
MNPs 1
Granulocytes
Pericytes
B cells 1
B cells 2
Fibroblast 2
Fibroblast 1
Erythro
Endothelium
CD8+ T
CD4+ T 2
CD4+ T 1
E)
H2-D1
H2-Ab1
Naive
Infected
Expression level
Nos2+ MNPs
Selenop+ MNPs
Ccl8+ MNPs
Chil3+ Cd11a+ MNPs
Cd11a+ MNPs
F)
Naive
30dpi
2.81%
4.22%
9.8%
36.8%
MHC-II-Qdot605
CD11b-PerCP-Cy5.5
G)
p = 0.01
% MHCII+ CD11b+
15
10
5
0
Naive
30dpi
H)
CellPhone DB: Cxcl signalling
MNPs 5
MNPs 4
MNPs 3
MNPs 2
Neurons
Neutro
DCs
MNPs 1
Pericytes
B cells 1
Granulocytes
Fibroblast 2
B cells 2
Fibroblast 1
Erythro
Endothelium
CD8+ T
CD4+ T 2
CD4+ T 1

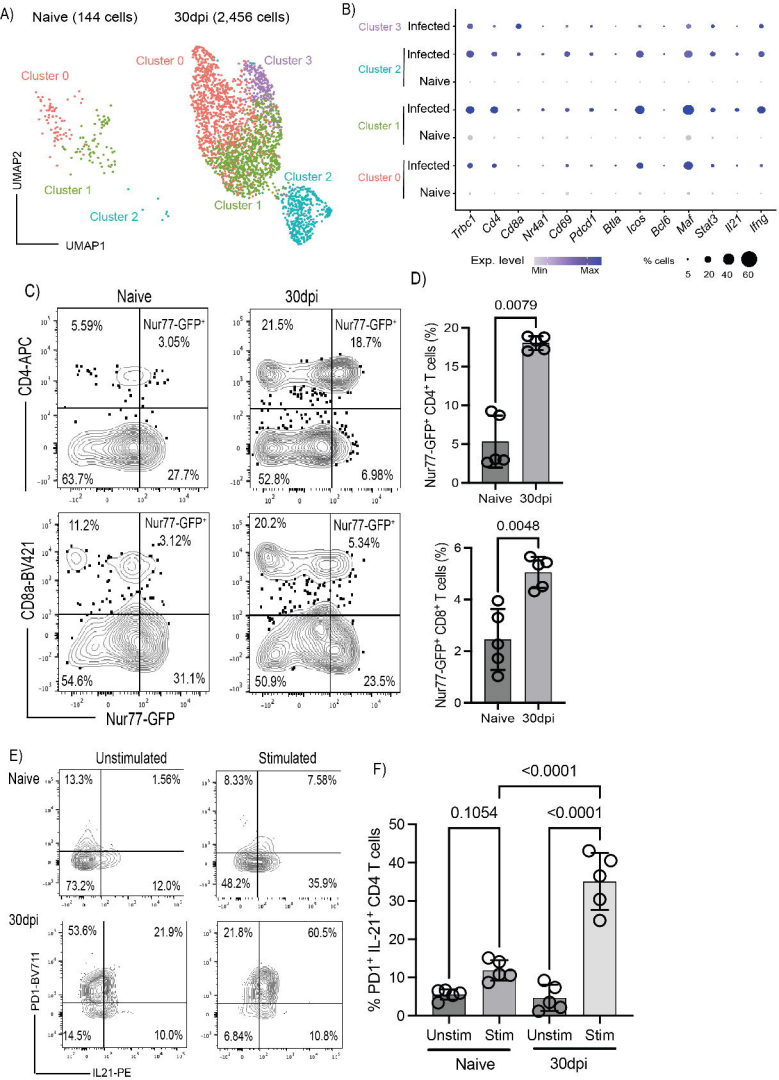
A)
Naive (144 cells)
30dpi (2,456 cells)
Cluster 0
Cluster 1
Cluster 2
Cluster 3
UMAP2
UMAP1
B)
Cluster 3
Cluster 2
Cluster 1
Cluster 0
Infected
Naive
Tnfrsf1
Cd4
Cd8a
Nr4a1
Cd69
Pdcd1
Btla
Icos
Bcl6
Maf
Stat3
Il21
Ifng
Exp. level
Min
Max
% cells
5
20
40
60
C)
Naive
30dpi
CD4-APC
CD8a-BV421
Nur77-GFP
5.59%
Nur77-GFP+
3.05%
63.7%
27.7%
21.5%
Nur77-GFP+
18.7%
52.8%
6.98%
11.2%
Nur77-GFP+
3.12%
54.6%
31.1%
20.2%
Nur77-GFP+
5.34%
50.9%
23.5%
D)
0.0079
Nur77-GFP+ CD4+ T cells (%)
Naive
30dpi
0.0048
Nur77-GFP+ CD8+ T cells (%)
Naive
30dpi
E)
Unstimulated
Stimulated
Naive
13.3%
1.56%
73.2%
12.0%
8.33%
7.58%
48.2%
35.9%
30dpi
53.6%
21.9%
14.5%
10.0%
21.8%
60.5%
6.84%
10.8%
PD1-BV711
IL21-PE
F)
<0.0001
0.1054
<0.0001
% PD1+ IL-21+ CD4 T cells
Unstim
Stim
Unstim
Stim
Naive
30dpi

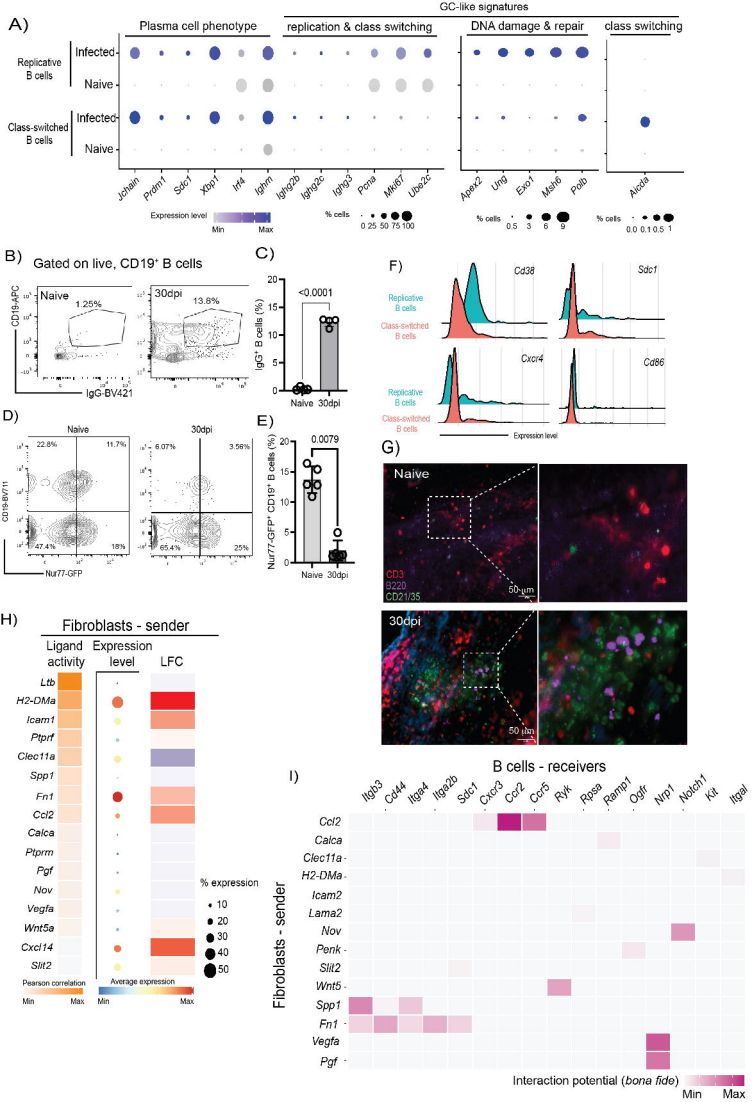
A)
GC-like signatures
Plasma cell phenotype
replication & class switching
DNA damage & repair
class switching
Replicative B cells
Class-switched B cells
Infected
Naive
Jchain
Prdm1
Sdc1
Xbp1
Irf4
Ighm
Ighg2b
Ighg2c
Ighg3
Pcna
Mki67
Ube2c
Apex2
Ung
Exo1
Msh6
Polb
Aicda
Expression level
Min
Max
% cells
0.25 50 75 100
0.5 3 6 9
0.0 0.1 0.5 1
B) Gated on live, CD19+ B cells
Naive
30dpi
1.25%
13.8%
CD19-APC
IgG-BV421
C)
<0.0001
IgG+ B cells (%)
Naive
30dpi
D)
Naive
30dpi
22.8%
11.7%
47.4%
18%
6.07%
3.56%
65.4%
25%
CD19-BV711
Nur77-GFP
E)
0.0079
Nur77-GFP+ CD19+ B cells (%)
Naive
30dpi
F)
Cd38
Sdc1
Cxcr4
Cd86
Replicative B cells
Class-switched B cells
Expression level
G)
Naive
30dpi
CD3
B220
CD21/35
50 µm
H)
Fibroblasts - sender
Ligand activity
Expression level
LFC
Ltb
H2-DMa
Icam1
Ptprf
Clec11a
Spp1
Fn1
Ccl2
Calca
Ptprm
Pgf
Nov
Vegfa
Wnt5a
Cxcl14
Slit2
% expression
10
20
30
40
50
Pearson correlation
Min
Max
Average expression
Min
Max
I)
B cells - receivers
Itgb3
Cd44
Itga4
Itga2b
Sdc1
Cxcr3
Ccr2
Ccr5
Ryk
Ropn
Ramp1
Odfr
Nrp1
Notch1
Kit
Itgal
Ccl2
Calca
Clec11a
H2-DMa
Icam2
Lama2
Nov
Penk
Slit2
Wnt5
Spp1
Fn1
Vegfa
Pgf
Fibroblasts - sender
Interaction potential (bona fide)
Min
Max

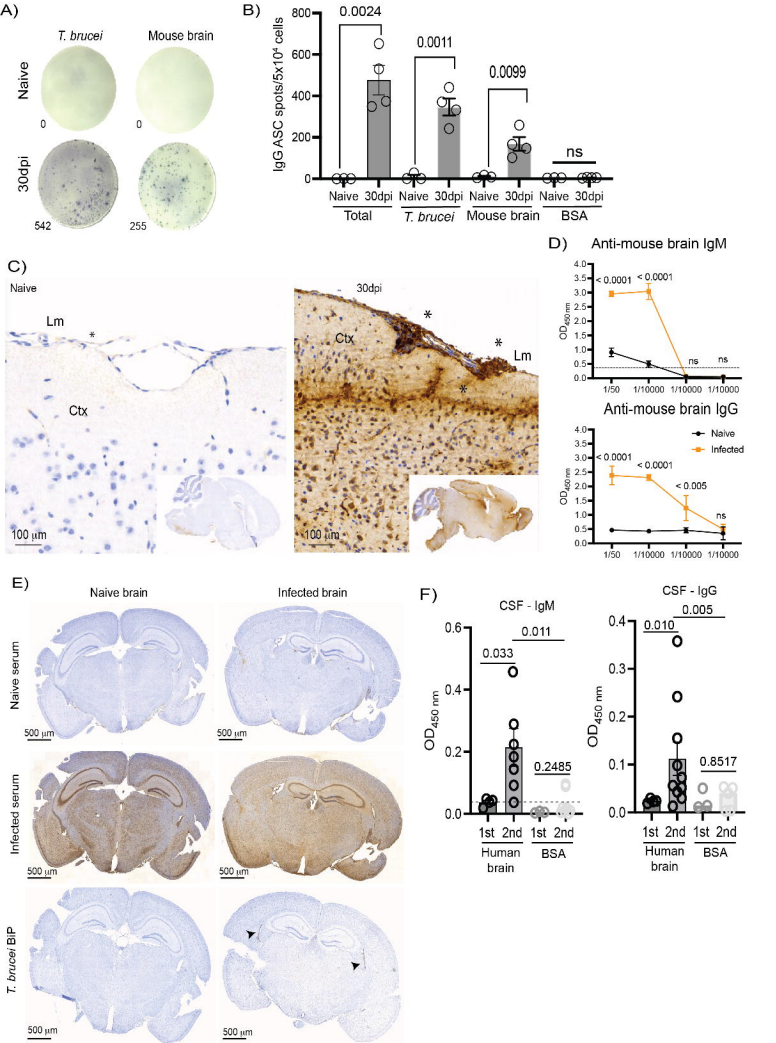
A)
T. brucei
Mouse brain
Naive
30dpi
0
0
542
255
B)
IgG ASC spots/5x10⁴ cells
0.0024
0.0011
0.0099
ns
Naive
30dpi
Total
T. brucei
Mouse brain
BSA
C)
Naive
Lm
Ctx
100 µm
30dpi
Ctx
Lm
100 µm
D)
Anti-mouse brain IgM
Anti-mouse brain IgG
OD450 nm
< 0.0001
< 0.005
ns
1/50
1/10000
Naive
Infected
E)
Naive brain
Infected brain
Naive serum
Infected serum
T. brucei BiP
500 µm
F)
CSF - IgM
CSF - IgG
OD450 nm
0.033
0.011
0.2485
0.010
0.005
0.8517
1st
2nd
Human brain
BSA

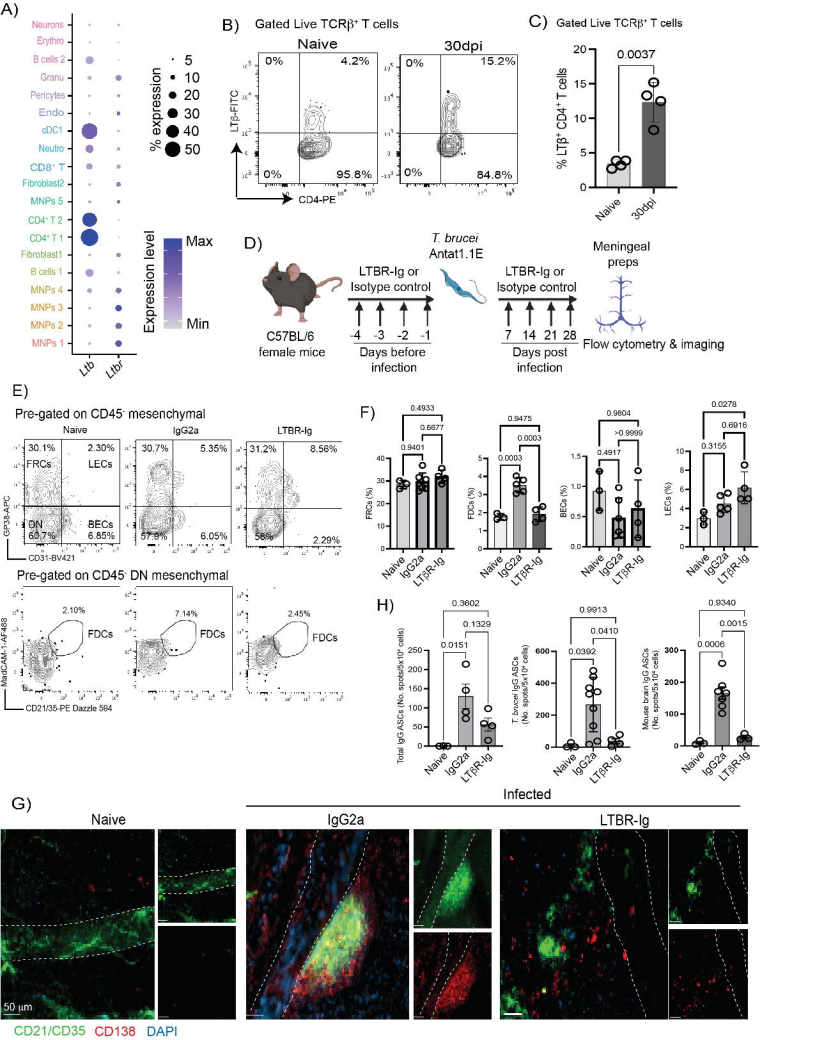
A)
Neurons
Erythro
B cells 2
Granu
Pericytes
Endo
cDC1
Neutro
CD8+ T
Fibroblast2
MNPs 5
CD4+ T 2
CD4+ T 1
Fibroblast1
B cells 1
MNPs 4
MNPs 3
MNPs 2
MNPs 1
Ltb
Ltbr
% expression
5
10
20
30
40
50
Expression level
Max
Min
B) Gated Live TCRβ+ T cells
Naive
30dpi
0%
4.2%
95.8%
0%
0%
15.2%
84.8%
0%
LTβ-FITC
CD4-PE
C) Gated Live TCRβ+ T cells
0.0037
% LTβ+ CD4+ T cells
Naive
30dpi
D)
C57BL/6
female mice
LTBR-Ig or
Isotype control
-4 -3 -2 -1
Days before
infection
T. brucei
Antat1.1E
LTBR-Ig or
Isotype control
7 14 21 28
Days post
infection
Meningeal
preps
Flow cytometry & imaging
E)
Pre-gated on CD45- mesenchymal
Naive
IgG2a
LTBR-Ig
30.1%
2.30%
FRCs
LECs
DN
60.7%
BECs
6.85%
30.7%
5.35%
57.9%
6.05%
31.2%
8.56%
58%
2.29%
GP38-APC
CD31-BV421
Pre-gated on CD45- DN mesenchymal
2.10%
FDCs
7.14%
FDCs
2.45%
FDCs
MadCAM-1-AF488
CD21/35-PE Dazzle 594
F)
0.4933
0.6677
0.9401
FRCs (%)
0.9475
0.0003
0.0003
FDCs (%)
0.9804
>0.9999
0.4917
BECs (%)
0.0278
0.6916
0.3155
LECs (%)
Naive
IgG2a
LTβR-Ig
H)
0.3602
0.1329
0.0151
Total IgG ASCs (No. spots/5x10^6 cells)
0.9913
0.0410
0.0392
T. brucei IgG ASCs (No. spots/5x10^6 cells)
0.9340
0.0015
0.0006
Mean brain IgG ASCs (No. spots/5x10^6 cells)
Naive
IgG2a
LTβR-Ig
G)
Naive
Infected
IgG2a
LTBR-Ig
50 µm
CD21/CD35 CD138 DAPI

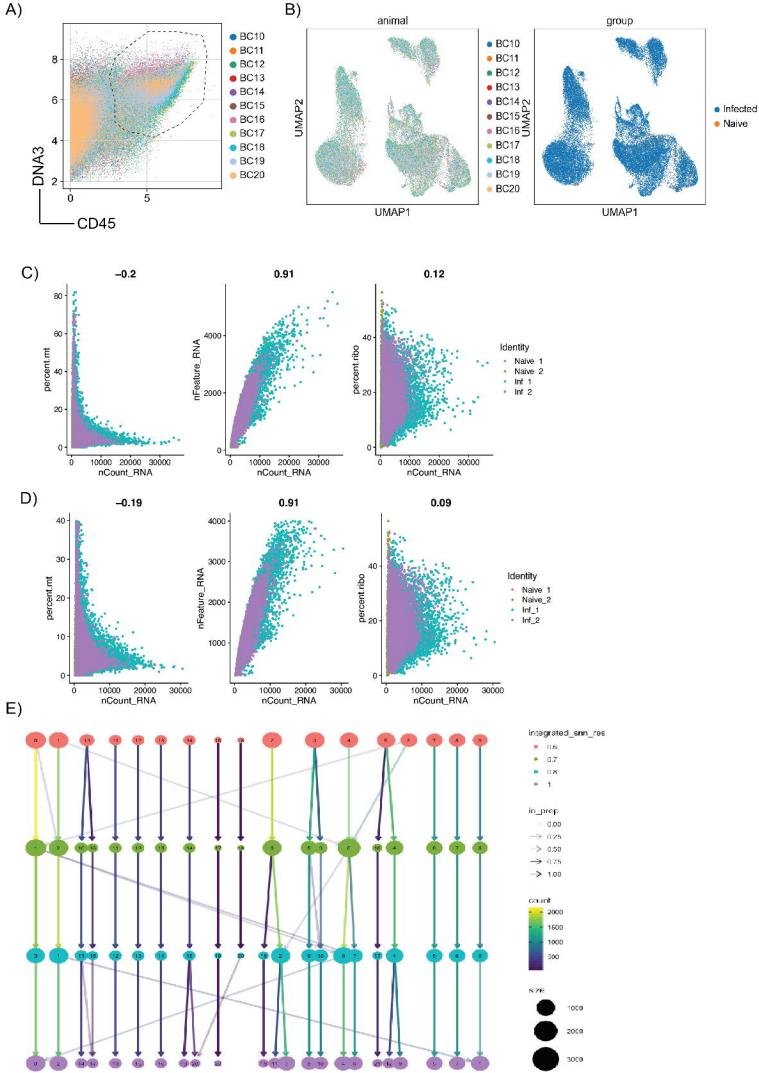
A)
DNA3
CD45
BC10
BC11
BC12
BC13
BC14
BC15
BC16
BC17
BC18
BC19
BC20
B)
animal
group
UMAP2
UMAP1
Infected
Naive
C)
−0.2
0.91
0.12
percent.mt
nFeature_RNA
percent.ribo
nCount_RNA
Identity
Naive 1
Naive 2
Inf 1
Inf 2
D)
−0.19
0.91
0.09
percent.mt
nFeature_RNA
percent.ribo
nCount_RNA
Identity
Naive_1
Naive_2
Inf_1
Inf_2
E)
integrated_snn_res
in_prop
count
size

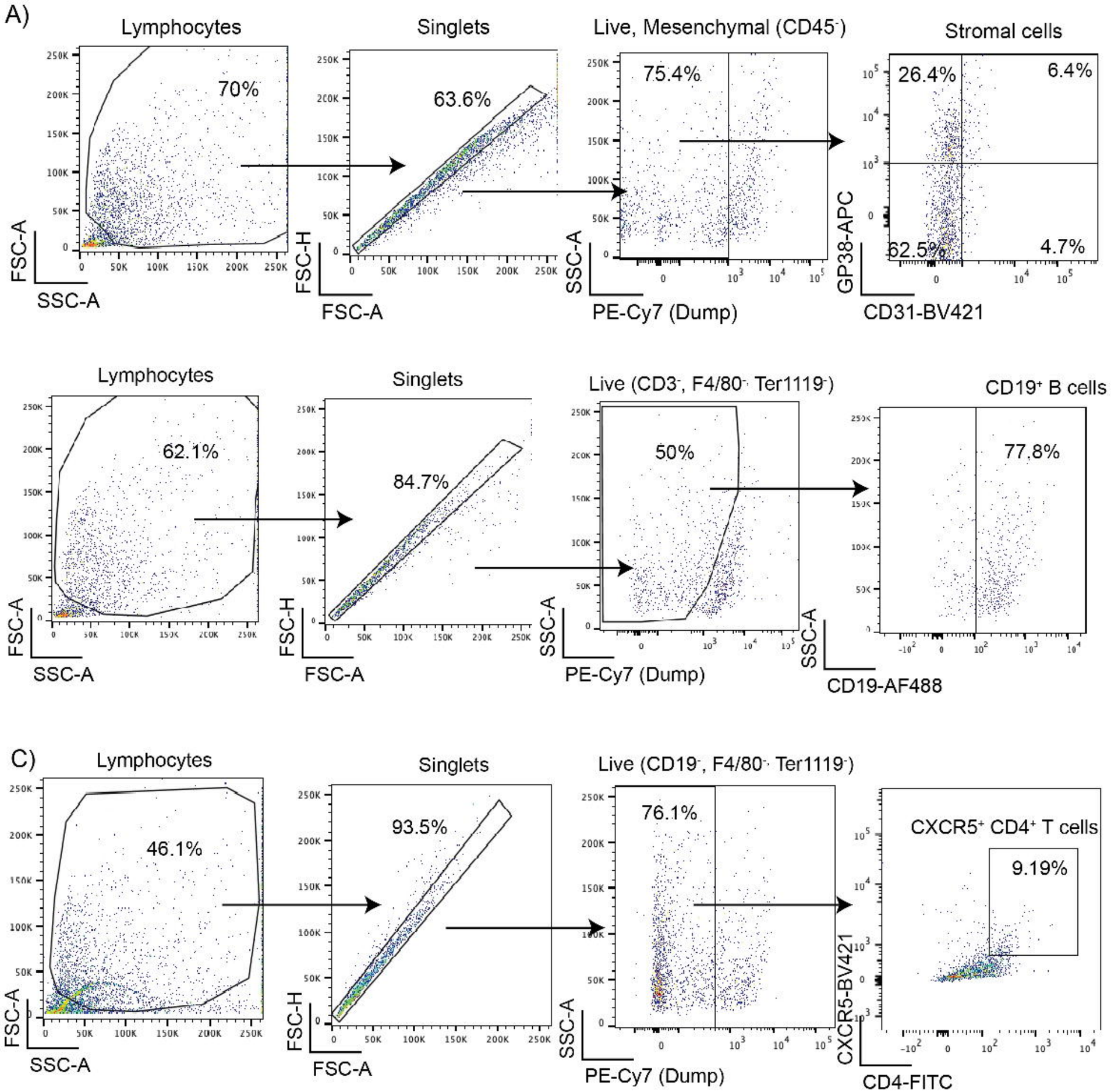
A)
Lymphocytes
70%
FSC-A
SSC-A
Singlets
63.6%
FSC-H
FSC-A
Live, Mesenchymal (CD45-)
75.4%
SSC-A
PE-Cy7 (Dump)
Stromal cells
26.4%
6.4%
62.5%
4.7%
GP38-APC
CD31-BV421
Lymphocytes
62.1%
FSC-A
SSC-A
Singlets
84.7%
FSC-H
FSC-A
Live (CD3-, F4/80- Ter1119-)
50%
SSC-A
PE-Cy7 (Dump)
CD19+ B cells
77.8%
SSC-A
CD19-AF488
C)
Lymphocytes
46.1%
FSC-A
SSC-A
Singlets
93.5%
FSC-H
FSC-A
Live (CD19-, F4/80- Ter1119-)
76.1%
SSC-A
PE-Cy7 (Dump)
CXCR5+ CD4+ T cells
9.19%
CXCR5-BV421
CD4-FITC

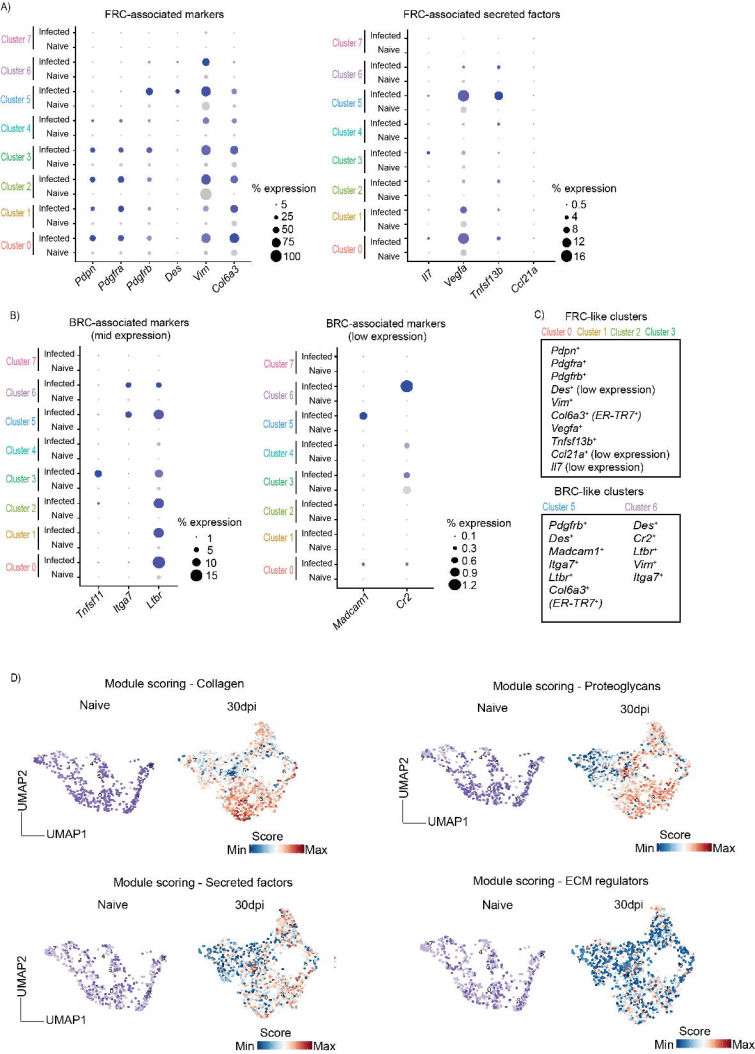
A)
FRC-associated markers
Cluster 7
Cluster 6
Cluster 5
Cluster 4
Cluster 3
Cluster 2
Cluster 1
Cluster 0
Infected
Naive
Pdpn
Pdgfra
Pdgfrb
Des
Vim
Col6a3
% expression
5
25
50
75
100
FRC-associated secreted factors
Il7
Vegfa
Tnfsf13b
Ccl21a
% expression
0.5
4
8
12
16
B)
BRC-associated markers (mid expression)
Tnfsf11
Itga7
Ltbr
% expression
1
5
10
15
BRC-associated markers (low expression)
Madcam1
Cr2
% expression
0.1
0.3
0.6
0.9
1.2
C)
FRC-like clusters
Cluster 0 Cluster 1 Cluster 2 Cluster 3
Pdpn+
Pdgfra+
Pdgfrb+
Des+ (low expression)
Vim+
Col6a3+ (ER-TR7+)
Vegfa+
Tnfsf13b+
Ccl21a+ (low expression)
Il7 (low expression)
BRC-like clusters
Cluster 5 Cluster 6
Pdgfrb+ Des+
Des+ Cr2+
Madcam1+ Ltbr+
Itga7+ Vim+
Ltbr+ Itga7+
Col6a3+
(ER-TR7+)
D)
Module scoring - Collagen
Naive
30dpi
UMAP2
UMAP1
Score
Min
Max
Module scoring - Proteoglycans
Module scoring - Secreted factors
Module scoring - ECM regulators

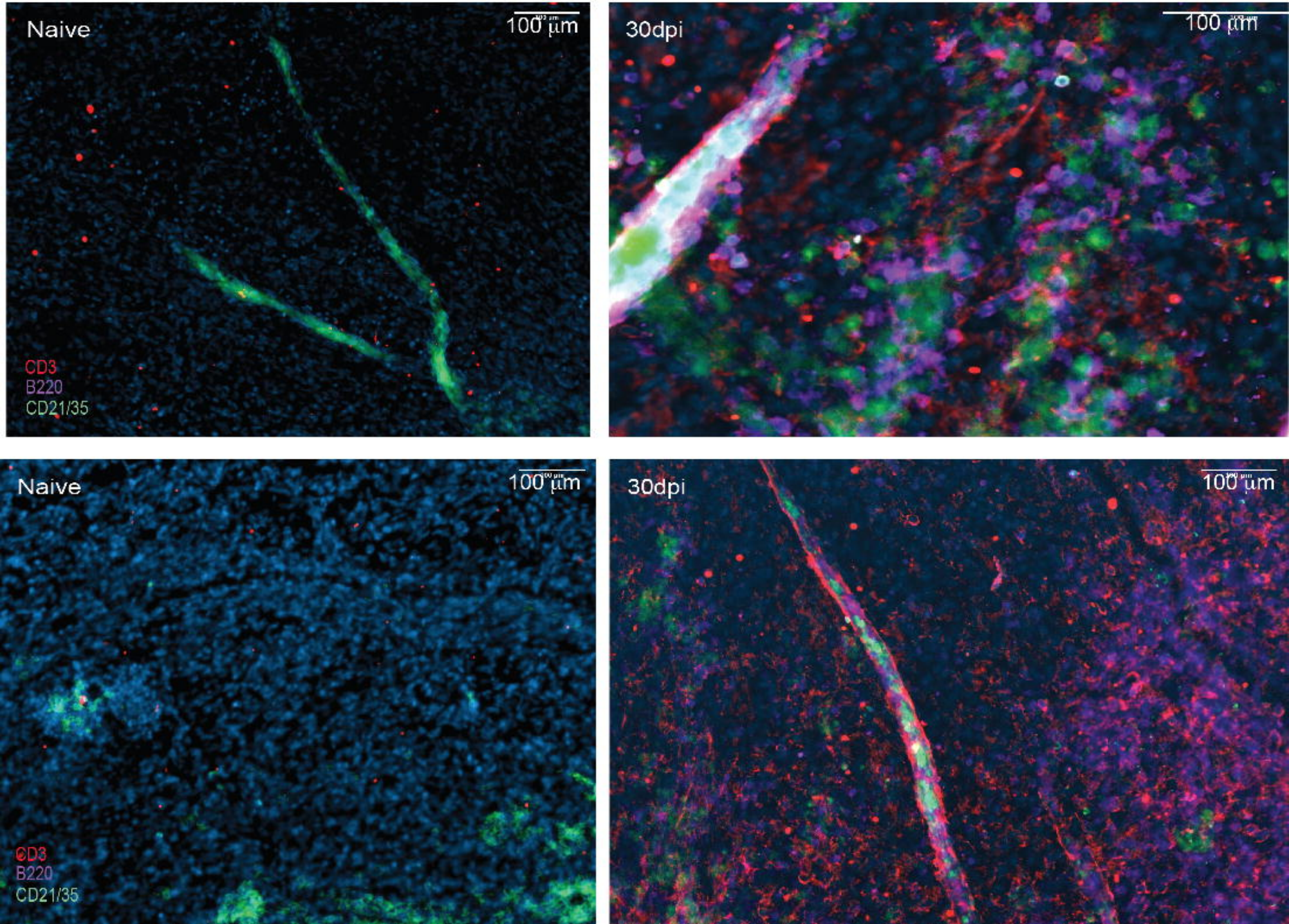
Naive
100 µm
CD3
B220
CD21/35
30dpi
100 µm
Naive
100 µm
CD3
B220
CD21/35
30dpi
100 µm

A)

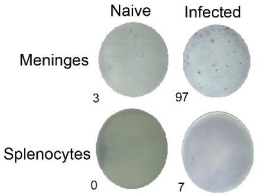

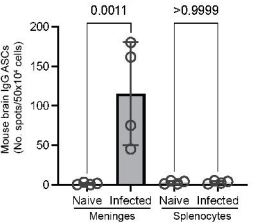

B) Naive brain

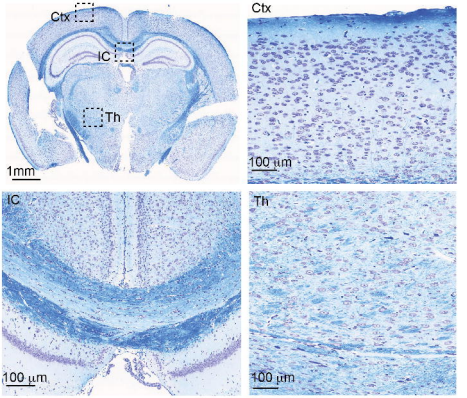

C) Infected brain

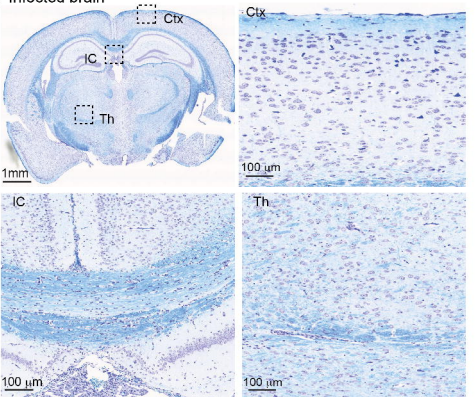

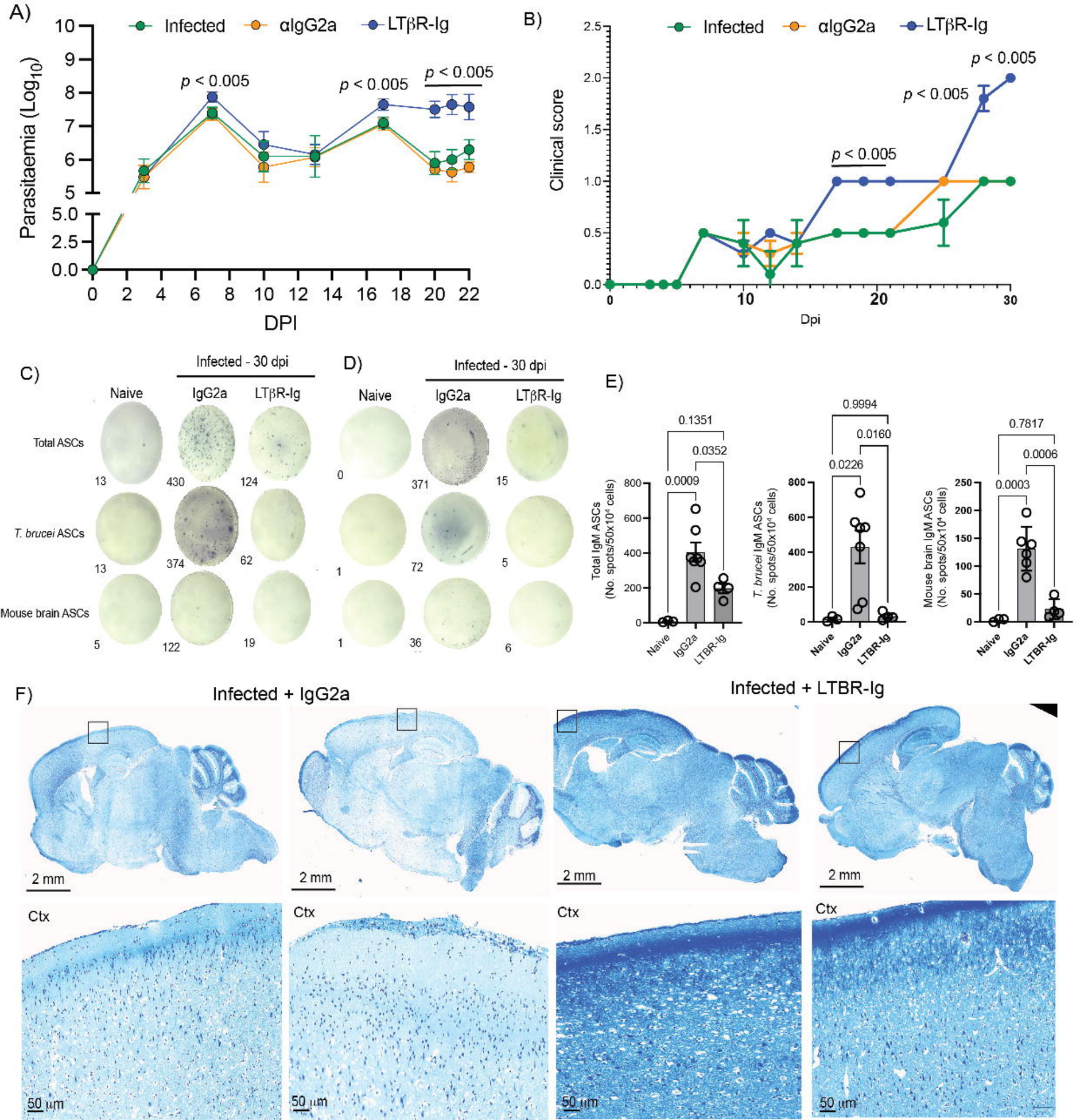
A)
Infected
αIgG2a
LTβR-Ig
Parasitaemia (Log10)
DPI
p < 0.005
p < 0.005
p < 0.005
B)
Infected
αIgG2a
LTβR-Ig
Clinical score
Dpi
p < 0.005
p < 0.005
p < 0.005
C)
Infected - 30 dpi
Naive
IgG2a
LTβR-Ig
Total ASCs
T. brucei ASCs
Mouse brain ASCs
13
430
124
13
374
62
5
122
19
D)
Infected - 30 dpi
Naive
IgG2a
LTβR-Ig
0
371
15
1
72
5
1
36
6
E)
Total IgM ASCs (No. spots/50x10⁴ cells)
T. brucei IgM ASCs (No. spots/50x10⁴ cells)
Mouse brain IgM ASCs (No. spots/50x10⁴ cells)
0.1351
0.0352
0.0009
0.9994
0.0160
0.0226
0.7817
0.0006
0.0003
Naive
IgG2a
LTBR-Ig
F)
Infected + IgG2a
Infected + LTBR-Ig
2 mm
Ctx
50 µm